Fibre-direction strain measurement in a composite ply under quasi-static tensile loading using Digital Volume Correlation and *in situ* Synchrotron Radiation Computed Tomography

E. Schöberl[1], C. Breite[2], A. Melnikov[2], Y. Swolfs[2], M. N. Mavrogordato[1], I. Sinclair[1], S. M. Spearing[1]

[1]Engineering Materials, Faculty of Engineering and Physical Sciences, University of Southampton,
Southampton SO17 1BJ, UK

[2]Department of Materials Engineering, KU Leuven, Kasteelpark Arenberg 44 box 2450, 3001 Leuven, Belgium

Keywords: Carbon-Fibre Reinforced Polymers (CFRPs), Microstructures, Micromechanics, Synchrotron Radiation Computed Tomography (SRCT), Digital Volume Correlation (DVC), Strain mapping

Abstract

Digital Volume Correlation (DVC), in concert with *in situ* Synchrotron Radiation Computed Tomography (SRCT), has been applied to Carbon-Fibre Reinforced Polymers (CFRPs) under quasi-static tensile loading. DVC represents a relatively novel tool for quantifying full-field volumetric displacements and implicit strain fields. The highly anisotropic and somewhat regular/self-similar microstructures found in well-aligned unidirectional (UD) materials at high volume fractions are shown to be intrinsically challenging for DVC, especially along the fibre direction. To permit the application of DVC to displacement and/or strain measurements parallel to the fibre orientation, the matrix was doped with a sparse population of sub-micrometre barium titanate particles to act as displacement trackers (*i.e.* fiducial markers). For the novel materials systems we have developed, measurement noise is considered along with the spatial filtering intrinsic to DVC data processing. Compared to volume images acquired through Micro-focus Computed Tomography (µCT), hold-at-load artefacts are mitigated through scan times on the order of ~seconds using SRCT, as opposed to ~hours. Instances of individually fractured fibres evolving into clusters of breaks are presented, together with the associated strain redistribution (imaged at a voxel resolution of 0.65 µm). It is shown that the distance over which strain is recovered in the broken fibres not only increases with the applied force, but also with the number of broken fibres, delineating aspects of the load shedding phenomenon. The study demonstrates that unprecedented, mechanistically-consistent three-dimensional (3D) strain measurements may be made in relation to fibre failure events, that can be used to validate micromechanical models for predicting UD tensile failure. We believe this work presents the first application of DVC to the SRCT imaging of failure in CFRPs, achieving significantly higher resolution than reported previously within the literature.

1. Introduction

Carbon-Fibre Reinforced Polymers (CFRPs) are increasingly used in transport applications due to their desirable strength- and stiffness-to-weight properties. The tensile failure of these materials involves a complex sequence of interacting mechanisms, including fibre-matrix interfacial debonding, matrix microcracking, delamination, fibre fracture, sub-laminate and ply failure. The interactions between the different mechanisms make it challenging to predict accurately the structural performance of composite materials. While the different mechanisms are important for the damage development and property degradation, the ultimate tensile failure of composite parts is generally recognised to be dominated by fibre fracture within 0° plies. Understanding the fibre fracture process is thus of fundamental importance for a complete interpretation of CFRP tensile failure, alongside the various other forms of composite damage that exist.

A key concept in longitudinal tensile failure of unidirectional (UD) composites is that fibre strength is a stochastic quantity [1], which is typically presumed to follow a Weibull distribution [2]. Therefore, fibre breaks are initially spatially distributed, and accumulate with increasing load. Around individual fibre breaks, the surrounding matrix transfers load, primarily in shear, into adjacent fibres [3], [4], [5], [6], [7], [8]. This stress transfer mechanism also reintroduces stress into the broken fibre, and the length over which this process occurs is commonly referred to as the 'ineffective length'. More specifically, Rosen [9] defined the ineffective length as twice the fibre length over which 90 % of strain recovery occurs. Complementary to this, is the 'overload length'; indicating the region over which the stress in immediately neighbouring filaments is increased. Nearby intact fibres will therefore carry local stress concentrations, but the magnitude decreases with increasing distance from the fibre break [10]. The stress (or strain) concentration factors (SCFs), defined as the relative change in the average stress (or strain) over the cross-section of an adjacent fibre due to the presence of a fibre break, is expected to increase the probability of fracture in these intact fibres [6], [10], [11], [12], [13]. With ongoing loading, this increased failure probability may lead to the development of clusters of breaks [13], [14], [15], [16], [17], [18], [19] which further increases the SCFs in the neighbouring fibres. Catastrophic failure is assumed to occur when sufficient neighbouring fibres are broken, and a critical cluster is formed, which grows in an unstable, self-sustaining manner [1], [10], [17], [19]. Therefore, apart from the fibre strength, the stress and strain redistribution around fibre breaks and the length over which it occurs becomes a key controlling parameter in predicting the tensile failure of UD composites. Raman spectroscopy [20], [21], [22], [23] represents a useful approach to perform such experimental measurements, however, it is limited to surface measurements, and has often been performed on model microcomposites with a sparse distribution of fibres, which may not exhibit fully-representative stress/strain states. Characterizing volumetric material deformation and damage in the bulk of practical specimens with realistic volume fractions thus becomes highly desirable. However, this is challenging, due to the opacity of the CFRPs, the three-dimensional (3D) multi-scale nature of damage, the coupling of multiple micromechanisms and the difficulty of distinguishing damage caused by cutting and polishing artefacts associated with metallographic sectioning [24].

A significant step forward has been achieved in recent years by the use of X-ray Computed Tomography (CT) combined with *in situ* loading to identify detailed sequences of damage accumulation down to fibre-level, in 3D, within the bulk of real engineering materials under load [13], [14], [18], [19], [25], [26]. It is then interesting to consider the use of Digital Volume Correlation (DVC) for a strain-based quantification of the local deformation surrounding fibre break sites in representative materials subjected to a continuously applied load. An extension of the white-light illumination, two-dimensional (2D) Digital Image Correlation (DIC) technique [27], DVC is a relatively novel tool capable of quantifying the internal microstructural response of the material between different load states, by extracting essential deformation and failure parameters such as local displacements and strains [24], [28]. Whilst not addressed here, applications to other aspects of composite micro- and mesomechanics may be envisaged, such as quantifying the influences of porosity or ply drops on local load paths/partitioning.

For X-ray CT, the noise and sensitivity of the DVC measurements rely on several factors. These include imaging hardware (beam stability, flux, energy, exposure, propagation distance, voxel size), the nature of the material type under investigation (sample shape, size, phase density distribution, trackable features) and imaging results (contrast-to-noise ratio, spatial resolution, artefacts), all of which influence the quality of the image volumes obtained [24], [29], [30]. Consequently, an assessment of the reliability and accuracy of the measurements is required through validation experiments for the imaging conditions in question, where the displacement and/or strain field is known *a priori* [24], [29]. In this context, Schöberl *et al.* [24] have reported a four-point flexural validation study, in which it was demonstrated that the DVC measurement of the bending strain gradient through the thickness of the specimen was in good agreement with the Euler-Bernoulli beam theory [31] for the current material. Additionally, the authors have undertaken error estimation by conducting two zero-strain pair analyses: a static repeat scan and a rigid body displacement assessment.

The underlying volume images for DVC are typically acquired through Micro-focus Computed Tomography (µCT) [24], [29], [30], [32], [33], [34], [35], [36], [37], [38], [39] or less frequently through Synchrotron Radiation Computed Tomography (SRCT) [37], [40], [41]. While both acquisition methods can deliver usable sub-micrometre voxel resolution levels, superior scans are commonly achieved through SRCT (the beam is brighter, monochromatic, coherent and parallel, with a higher level of phase contrast and avoids beam hardening artefacts [42]). Furthermore, µCT is characterised by significantly longer scanning times on the order of ~hours, as opposed to ~seconds for SRCT [42], particularly at sub-micrometre resolutions. This may be expected to promote hold-at-load artefacts near composite failure, whereby the viscoelastic response of the polymer matrix may result in time-dependent strain variation and subsequent failure of UD composites [43], [44], [45], [46].

Unlike many monolithic materials (*e.g.* Al-Si alloys), which contain well-distributed, small inclusions which provide X-ray contrast [37], the highly anisotropic and somewhat regular/self-similar microstructures found in conventional unidirectional CFRPs at high volume fractions are intrinsically challenging for DVC, particularly along the fibre direction. The cylindrical structure and relatively featureless surfaces of the filaments lack a well-defined, trackable contrast pattern along the fibre direction, leading to poor image correlation, and correspondingly inaccurate displacement estimates in this direction within a given ply [40]. Following a similar approach to that taken by Brault *et al.* [34] to generate individual features unique to a particular sub-set, the authors have doped the matrix with a sparse population of particles (but significantly smaller, at 400 nm *vs.* 150 µm used in [34]) to act as displacement trackers – *i.e.* fiducial markers [24]. High-resolution, fibre-level strain distributions are specifically addressed (imaged at a voxel resolution of 0.65 µm), as opposed to the ply-level studies in [34]. The fraction of fiducial markers is selected such that any potential impact on the mechanical performance of the material is mitigated. Previous studies have shown that for low particle concentrations, the mechanical properties of thermosetting matrices can be largely preserved [47], [48]. In turn, by comparing the micromechanical behaviour of the particle-adapted material alongside its particle-free counterpart, we demonstrate elsewhere [49] that the response of the newly developed CFRP is consistent with standard production materials suggesting its suitability as a model system for mechanistic investigations.

Using this approach, we report *in situ* SRCT tensile testing and micromechanical strain mapping results for the regions immediately surrounding fibre breaks. A complex load shedding phenomenon is identified at fibre-level, whereby the distance over which strain is recovered in the broken fibre not only increases with the applied force, but also with the number of broken fibres. For the first time, key 3D strain measurements around fibre breaks have been made that can be compared to micromechanical Finite Element (FE) models. The work is intended to support material development and promote the understanding of the fundamental aspects of unidirectional composite tensile failure.

2. Materials and methods

2.1. Material manufacturing

Cross-ply laminates, with a $[90/0]_s$ layup, thickness of ~1 mm and a specimen fibre volume fraction (V_f) of ~55 % were manufactured by drum winding at KU Leuven, Belgium. A polyacrylonitrile-based (PAN) 12K TORAYCA T700SC-50C (Toray Industries Inc., Tokyo, Japan [50]) non-twisted tow was used, with a 7 µm nominal fibre diameter.

To create microstructural fiducial patterns for the application of DVC, the resin was filled with commercially available tetragonal $BaTiO_3$ particles, nominal mean size of 400 nm and approximately spherical shape (US Research Nanomaterials Inc., Houston, TX, USA [51]). This property combination was selected following an extensive µCT-based qualitative assessment on a range of possible fiducial compositions (Al, Al_2O_3, SiC, SiO_2, MgO, TiC, TiO_2, $BaCO_3$, $BaTiO_3$, Cu and Bi_2O_3), mean particle sizes (300 nm to 800 nm) and concentrations (0.25 wt. % to 15 wt. % of the resin). From this test matrix, $BaTiO_3$ particles were found to offer the most favourable compromise between contrast in CT images (high attenuation coefficient), and the ability to obtain a homogeneous distribution in 3D space with sufficient particle compactness for local DVC analyses. The particles were dispersed in a SiPreg KTA 313/SR 8500 dual-component epoxy (Sicomin, Châteauneuf-les-Martigues, France [52]) using a combination of high-shear mixing and heated ultra-sonication (U100H bath, Ultrawave Ltd., Cardiff, UK [53]). No specific treatment was applied to the particle surfaces. To remove entrapped air, the thermosetting mixture was degassed for 10 minutes at ambient temperature. The amount of resin used was 150 g, with 31.5 g of hardener, following the manufacturer's specified mixing ratio of 100/21 (by weight). The $BaTiO_3$ fraction was set at 7.5 wt. % of the resin, equivalent to ~1.44 vol. %. A nominal 25 % tow overlap was targeted during the winding process. A maximum spool tension of 0.12 lb (54.43 g) was applied. To control the volume fraction of the matrix, following impregnation, the tow was passed through a metering die with an orifice slot of 0.2 mm × 9 mm. The temperature of the tow spreader and final guide roller were set to 50℃. The fibre sizing was left intact. For a schematic diagram of the manufacturing setup, the reader is referred to [24]. The drum winding process resulted in uniaxial prepreg tape, ~0.25 mm × ~350 mm × ~1900 mm, which was cut and laid up to produce the desired $[90/0]_s$ cross-ply layup. The prepreg stack was cured in an autoclave for 280 minutes at 0.5 MPa (5 bar) and maximum 120℃. To minimize void content in the cured material, a vacuum of ~0.07 MPa (~0.7 bar) was maintained throughout the autoclave process.

2.2. Specimen geometry and loading

Double-edge notched specimens were machined via water-jet cutting. The specimen geometry is based on previous work of Swolfs, Scott, Garcea, Rosini, Moffat, Wright and co-workers [13], [14], [15], [18], [19], [25], [26], although here the total specimen length was increased to 100 mm, as reported in [19]. This was performed to (a) minimize the risk of pull-out from the central 0˚ portion of the gauge region, and (b) to accommodate a smaller X-ray propagation distance, by providing sufficient clearance between the top of the loading rig and detector optics. Once cut, the T-shaped sections of the specimens were tabbed with 1.5 mm thick aluminium sheet. Aerospace-grade adhesive, Scotch-Weld EC-9323 B/A (3M Company, Maplewood, MN, USA [54]), was used to bond the tabs onto the CFRP surface. Adhesive curing was performed at 65°C for 2 hrs according to the manufacturer's recommendations. The key specimen dimensions, the tabbed assembly and the highly contrasted microstructure are collectively shown in **Fig. 1**. Tensile loading was performed *in situ* by using a modified CT5000 single-actuator electromechanical rig (Deben Ltd., Woolpit, Suffolk, UK [55]) retrofitted with a Poly(Methyl Methacrylate) – PMMA reaction tube (25 mm outer diameter and 3 mm wall thickness). Using position control to ameliorate potential artefacts during scanning, loading was performed at a displacement rate of 0.2 mm/min up to a prescribed load point. Typically, ten load steps were applied for stepwise *in situ* measurements, with somewhat smaller load increments being made at high loads, close to failure. This was applied on the basis of the work of Scott *et al.* [14], where fibre breaks have been confirmed to accumulate exponentially with applied stress, with the majority of breaks occurring above ~90 % UTS. To alleviate potential effects of specimen relaxation under load (and thus potential movement during CT acquisition), scanning was carried out with a slight reduction in load (~10 %) from the most recent peak level applied. It is also worth stating that at the scale we are observing, the fact that the fibres are in a cross-ply have no effect on the fibre-scale stress transfer characteristics, as shown in [13] and [14]. That is because splitting and delamination does occur, which essentially creates a local UD composite in the notched region of the specimen after a certain strain (typically ~70% UTS [14]). Noise and sensitivity assessment scans (static repeat and rigid body displacement) for the DVC technique were conducted with a small applied preload, max. 75 N, to ensure that the specimen did not move during acquisition and/or manipulator stage translation.

2.3. Synchrotron Radiation Computed Tomography

In situ SRCT measurements were performed at the ID19 beamline, European Synchrotron Radiation Facility (ESRF), Grenoble, France. A 2560 × 2160-pixel detector was used, with a chip size of 6.5 µm. Scans, with a monochromatic beam, were conducted at a 10x magnification, yielding a voxel size of 0.650 µm and a field of view (FOV) of ~1.66 mm × ~1.40 mm × ~1.66 mm. The beam energy was set to 19 keV, with 2996 projections acquired per scan, at an exposure of 25 ms, resulting in ~75 s per tomograph. Acquisition was performed over a rotation of 180°. A propagation distance of ~30 mm was used, while the data was reconstructed using conventional absorption-based Filtered Back Projection (FBP).

2.4. Digital Volume Correlation

Digital Volume Correlation was performed using the commercial DaVis v10 software with StrainMaster DVC package (LaVision GmbH, Göttingen, Germany [56]). StrainMaster employs a correlation criterion operating on the grey-level intensity values of 3D images [41]. In essence, the measurement volume is divided into smaller sub-sets, and the contrast pattern within each sub-set is then tracked from the reference to the deformed state independently (local approach [33]) as a discrete function of the grey-levels [41]. A cross-correlation function is employed to measure the conservation of the grey-levels between the original and displaced sub-set, with the position determined for which the correlation is closest to unity [24], [30], [40], [41]. Analogous to DIC, the correlation coefficient can be used to evaluate the similitude between the sub-sets [24], [30]. A coefficient of 1.0 implies that the sub-sets are completely related, whereas a value of 0 indicates that they are completely unrelated [24], [30].

The correlation process between two adjacent volumes ‘A’ and ‘B’ is illustrated schematically in **Fig. 2**, which is complemented by the workflow diagram in **Fig. 3**. The associated shift (3D displacement) is given by the vector connecting the sub-set centroids between the deformation states [56]. Finally, 3D strain field estimation may be carried out through a centred finite difference to determine the numerical derivatives of the vector field [24], [30], [35], [41], [57].

Recognition of matching sub-sets between the deformation states was performed within the DVC software either via a Fast Fourier Transform (FFT) implementation, referred to as ‘FFT’, or via a multi-step strategy whereby a global pre-shift was computed through the ‘FFT’ approach, followed by Direct Correlation – ‘DC’. Both implementations use an equivalent of a piece-wise linear shape function for the reference-deformed mapping, a normalized form of the cross-correlation function to quantify the similarity between the images, and support a multi-pass approach [30], [36], [41], [56]. A trilinear interpolation is used in ‘FFT’, and a third-order spline interpolation in ‘DC’, to compute the greyscale intensities of each displayed voxel at non-integer positions (*i.e.* sub-voxel measurements) [36]. ‘DC’ also permits the use of a weighted window within sub-sets, an option which was implemented during the final iteration step of correlation (dual-pass). This results in a potentially improved representation of the local displacement field, as the voxels in the vicinity of the sub-set centroid carry more weight than voxels located at the edge of the sub-set. While the weighted window extends over two times the sub-set size, the implementation ensures that the effective spatial resolution is similar to that of a conventional sub-set, for which an arithmetic average is implemented [56]. As isotropic sub-sets were used throughout all present analyses, a specific notation is introduced, whereby the specified size of a sub-set is equivalent to a sub-set with its characteristic length cubed (*i.e.* sub-set size of N voxels is equivalent to a sub-set size with $N \times N \times N$ voxels or N^3 voxels). More information on LaVision’s DVC implementation can be found in [30] for the ‘FFT’ and in [41] for the ‘DC’ method and/or by consulting the software guidelines [56].

The ‘DC’ approach can maximise the efficiency of using the DVC algorithm, as the search for the corresponding sub-set in the deformed state was confined to a shift equal to the search radius. Additionally, in ‘DC’ the coarse displacements, captured by using larger sub-sets, were used as a predictor vector field for the subsequent and refined iterations, based on smaller sub-sets. Although the latter implementation is also possible using ‘FFT’, the additional steps can outweigh the faster processing times associated with the frequency domain. Following a comprehensive parametric study and algorithm optimization process respectively, it was established that ‘DC’ yields generally superior performance in terms of noise and sensitivity. As a result, the direct correlation method was used throughout this work.

To moderate computational costs, two further strategies were used. First, a 32-bit floating point to 8-bit integer conversion was performed for the voxel data. While the correlation results will always be imaging configuration-dependent, Buljac *et al.* [58] have shown that histogram (grey-level) rescaling has negligible impact on the DVC error. Similarly, the bit-depth of volumes was also reduced in [40] to achieve faster processing times. Secondly, for the direct correlation method, the search radius was incrementally reduced from 8 to 6 and ultimately 4 voxels between the deformed and undeformed state. The latter value corresponds to a typical fibre-break opening (based on a 0.65 μm voxel size) in a T700SC-50C/epoxy-based cross-ply, implying that in the absence of fractured fibres and/or matrix microcracks within the 0° plies, the elastic response of the microstructure cannot exceed the aforementioned displacement level. Nonetheless, for very small sub-set sizes and large clusters of breaks, a higher search radius may be required to fully characterise the local deformation.

To increase sampling, the overlap between the neighbouring sub-sets was set to 75 %. This represents a higher sampling rate than that previously reported in [24], [30], [35], [40], for which a 50 % sub-set overlap was used. Correlation was carried out relative-to-first, *i.e.* each volume was correlated with the initial undeformed scan. The relevant settings used are detailed in **Table 1.**

To assess the noise and sensitivity associated with the DVC technique, conventional stationary and rigid body displacement tests were performed. DVC was applied to cropped volumes from the 0° plies, measuring 600 × 600 × 600 voxels. Gross rigid body displacements were initially removed by carefully cropping the volumes with a voxel accuracy. As previously indicated in **Fig. 1**, the Y-axis indicates the fibre direction, the X-axis is in-plane orthogonal to the fibre direction, while the Z-axis corresponds to the out-of-plane direction. Volumes were carefully checked against the presence of any significant CT artefacts (*e.g.* rings, streaks) and/or variations in sharpness within the visible region.

As summarized in **Table 2**, the number of DVC 'slices' (*i.e.* planes composed of volumetric sub-sets, one sub-set thick) is computed by dividing the height of the cropped volume (*e.g.* 600 voxels) by the step size used in the correlation algorithm. Such an example is illustrated in **Fig. 4**, where a stack comprising of 33 DVC slices can be observed. As the in-plane voxel dimensions are equivalent (*i.e.* 600 × 600 voxels), the same number of DVC data points is obtained in-plane as per the slices in **Table 2**.

Sub-sets positioned at the perimeter of the grid (XY-plane) as well as the planes of sub-sets located at the top ends of the stack (Z-direction) must be treated with special consideration (*e.g.* masked or truncated) if displacement vectors are computed, but not 100 % satisfied from a voxel validity perspective – *i.e.* notional sub-sets that overlap with the edge, due to cropping between deformation states and/or large rigid body displacements, potentially causing the correlated data to be noisier or incomplete [24], [35].

A common post-processing aspect of strain computation via DVC (and related DIC algorithms) is the Virtual Strain Gauge (VSG). The VSG defines the local (effective) region of the image that is used for strain calculation at a specific location and is volumetrically analogous to the physical area that a foil strain gauge covers [57]. Additionally, the VSG may also be considered to be a smoothing/noise-removal strategy as it represents a higher-order filtering stage for the computed strains. More details about the application of VSGs can be found in [57].

Several key variables affect the VSG size, such as the characteristic length (size) of the: strain window (L_{SW}), step (L_{ST}) and sub-set (L_{SS}). As the characteristic length (L_{VSG}) of the VSG decreases, the noise typically increases, as the amount of global spatial filtering decreases. Similarly, as the size of the VSG decreases, the apparent magnitude of local strain peaks along a line cut (extracted region of highest strain gradient) may be generally expected to increase [57]. In this paper, a VSG with an L_{SW} of 3 × 3 × 3 neighbouring vectors was used, unless otherwise stated (**Fig. 5**). The application of a VSG implies that the effective volumetric gauge-length over which each strain value is computed is larger than the size of a single sub-set [24], with **Equation 1** describing how the characteristic length of the VSG scales with the aforementioned parameters [57].

$$L_{VSG} = (L_{SW} - 1) \times L_{ST} + L_{SS}$$

Equation 1

3. Results and discussion

3.1. Noise and sensitivity

As noted above, to evaluate quantitatively the performance of the DVC technique, noise studies were conducted. The assessment involves two studies, with the approach being similar to that of Schöberl *et al.* [24], Gillard *et al.* [30], Pierron *et al.* [35] and Borstnar *et al.* [40]. The first is a stationary analysis, which involves repeated scanning of the same specimen without any alterations in load (zero displacement, zero strain) or CT parameters (exposure, number of projections, beam energy, current or propagation distance). The purpose of this static noise test (SNT) is to quantify the intrinsic scanning noise and bias. The second study is a rigid body displacement (RBD) in which the specimen was moved *in situ* by a predefined displacement, parallel to the fibre direction (Y-axis), using the manipulator stage. CT acquisition was performed between each specimen position to evaluate the magnitude of the displacement vector fields and to assess any interpolation and/or system errors associated with the DVC approach [40]. For a detailed analysis, the reader may consult **Appendix A** to **C**.

3.2. Strain field assessment at single fibre breaks

As stated in **Section 2.4.**, a key aspect of the DVC technique is that the resulting measurements must be regarded as a spatially filtered representation of the real local strains within the material. As such, the deformation captured is affected and/or limited by the volume that is used for strain calculation at a specific location within the material. Since the interest here lies in capturing the strain field longitudinally from a fibre break, a suitable approach is to create a computational domain that isolates the fibre break opening. The rationale is that there can be no strains where there is no material [40] (*e.g.* fibre break openings, cracks). Additionally, no meaningful correlation can be performed between ‘non-material’ at a break site, and the original material microstructure. An algorithmic mask (proprietary [56]) was thus applied to the cropped data, whereby all voxels with a grey-level below a threshold corresponding to the break opening (50/255) have been excluded from the computational domain. Therefore, the values quoted in this section refer to the average strains derived from the sub-set centroid shifts, where only voxels exceeding the aforementioned grey-levels have been incorporated. The disadvantage of this technique is that voids are also masked, and thus fail to assist the correlation algorithm. Nonetheless, the impact is considered negligible due to the low content of voids within the manufactured CFRP.

3.2.1. Strain transfer lengths

Fig. 6 presents a representative measured strain map overlaid with the microstructure subjected to *in situ* loading at the 950 N load step. The FOV was centred on a singlet, labelled ‘C’. A singlet is defined in this work as a non-interacting break, separated by at least ten fibre diameters longitudinally (Y) and two fibre diameters radially (X & Z), measured from the centre of the nearest neighbouring break.

To make best use of the spatial resolution attainable, correlation was performed with the smallest workable sub-set size of 32 voxels (20.8 µm) and 75 % overlap, yielding a step size of 8 voxels (5.2 µm). Similarly, to limit smoothing in the fibre direction, strain post-processing was performed with a strain window size of 1 × 3 × 1 vectors, resulting in a VSG size of 32 × 48 × 32 voxels. A conversion to physical units and/or equivalent fibre diameters is available in **Appendix C**.

The numerical data, based on centroid-to-centroid measurements, was extracted from the overlapped sub-sets best aligned with the centre of a fractured carbon-fibre. Longitudinally from the break plane, the DVC output yields two near-symmetrical and distinct strain regions – **Fig. 6**: (1) an ‘elevated strain length’ measuring ~16 µm – where the strain drops from the maximum recorded value of ~4.85 % to ~zero, and (2) a ‘lower strain length’ of ~21 µm – where the strain gradually increases from ~zero to the far-field measurement of ~1.5 %. Combined, these strain transfer lengths may be identified with a ‘recovery length’ from one side of the break, with the ‘full-recovery length’ being approximatively twice this value.

Fig. 7 presents a line plot of strain (ε_{yy}) from the bottom side of a break, where half of the ‘full-recovery length’ is differentiated as described above. The results are expanded in **Fig. 8**, where a collection of measurements from eight identified singlets (‘A’ to ‘H’) is shown, with the strain data extracted from both sides of the break plane (*i.e.* ‘full-recovery length’). Good consistency can be observed between the different measurements, where slight deviation from symmetry for some of the gradients may be attributed to measurement noise, microstructural variations or somewhat different damage evolution mechanisms on opposite sides of the break plane. It is also worth noting that no correlation was found between the broken fibres and high concentration regions of particles.

Given the effective gauge length/volume of strain measurements, it is of course clear that apparent strains will be influenced by crack/break displacements. As such, the ‘recovery length’ computed via DVC does not follow a typical Cox [59] (shear-lag) profile, which predicts that the strain should fall to zero at the fibre ends. While this may be asserted for measurements that are strictly referred to fibres [10], [11], [12], it must be noted that the DVC-estimated strains reflect the spatial filtering associated with the technique. Remote from local discontinuities/cracks, microstructural anomalies and/or other sources of strain gradients, it may be expected that the Voigt [60] isostrain assumption applies to the material and the strains reported by DVC are a good estimate of both fibre and matrix deformation; with the latter being the dominant contributor, as it contains the fiducial markers used to achieve reliable correlation (**Appendix A**). However, immediately adjacent to fibre breaks, steep strain gradients are expected, and may be influenced by the following mechanisms, or combinations thereof: (1) matrix plastic yielding [21], [22], [23] (2) fibre-matrix interfacial debonding (with slippage) [22], [23], [61], [62], [63], [64] (3) matrix microcracking [64], [65], [66], [67], and (4) fibre unloading and spring-back [3], [68], [69], [70]. The relative displacement of the edge-enhanced fibre ends [42] is also expected to contribute to the measured strain field.

Along with the matrix deformation, the local strain profile longitudinal from the broken fibre measured by DVC is therefore in fact a superposition of two profiles widely noted in the literature: (1) the 'ineffective length', which is widely defined in the modelling literature as twice the distance from the break plane over which the strain is recovered to a certain percentage in the broken fibre [9], [10], [11], [12], [13], and (2) the 'overload length' of the intact fibres associated with the length over which the stresses are increased due to the presence of a fibre break. The DVC-based 'lower strain length' is observed to follow the profile of the former, while the 'elevated strain length' may additionally encompass the 'overload length' or twice the distance between the break plane and the plane at which the intact fibre has an SCF of 0 % [10], [11], [12], [13]. Progressing onwards from the 'recovery length', ∼37 µm away from the break plane, the deformations are likely to be entirely elastic.

It is, however, recognized that fibre-matrix interfacial debonding cannot be directly observed in the present experiment, nor in other state-of-the-art *in situ* SRCT works [13], [14], [15], [18], [19], [71]. The two debonded surfaces stay in close contact, making it impossible to detect them with CT at voxel resolutions of ∼0.65 µm [1]. Nonetheless, surface experiments (*e.g.* based on Raman spectroscopy [22], [23] and/or photoleasticity [61], [62], [63], [64]) report that such damage mechanisms take place under specimen tensile loading, albeit in model microcomposites with a sparse fibre distribution. Whether the knowledge from microcomposites can be reliably transferred to macro-composites containing bundles of fibres remains unknown [1].

Radially from the centre of the break plane, the strain transfer lengths are observed to fall-off incrementally. **Fig. 9** presents the strain profile from singlet 'F', whereby the data was collected longitudinally from both sides of the break plane, with the measurements being repeated stepwise in the transverse direction (X). Beyond a radial distance of ∼26 µm or the equivalent of ∼four fibre diameters, it is observed that the strain gradients are significantly reduced, and the far-field strain reading of ∼1.5 % is reached. Although not shown here, owing to the 3D capabilities the data may also be interpreted in the out-of-plane direction (Z), where the strain distributions follow a very similar profile. This implies that the volume of material surrounding a single fibre break measures ∼52 µm × ∼74 µm × ∼52 µm, within which load shedding takes place, increasing the probability of fibre break (or cluster) development. Very similar results are found at each of the eight single fibre break sites investigated.

3.2.2. Effect of applied load on strain transfer lengths

Using Rosen's [9] definition of the ineffective length (twice the fibre length over which 90 % of strain recovery occurs), the effect of applied load on the DVC-based 'full-recovery length' is illustrated in **Fig. 10 (a)**. The strain gradients are compared at the 950 N and 900 N load steps respectively, with the effect discussed on an average basis. This strategy is employed to resolve the discrepancies from **Fig. 8**. The eight singlets ('A' to 'H') identified in **Section 3.2.1.** were used to compute a mean strain distribution at the last loading step, while four singlets could be traced back ('A', 'B', 'D', 'F') to the preceding loading step; with the remaining four singlets spontaneously appearing during specimen loading to the ultimate load step of 950 N. One singlet ('A') could be traced back to two preceding loading steps from 950 N; namely 900 N and 850 N. These results are shown separately in **Fig. 10 (b)**, noting the quantitative evaluation exceeds that of the measurement noise. Below this load step, the carbon-fibres are predominantly intact, which limits the analysis to a relatively narrow range. As in the previous section, strain gradients at fibre breaks were post-processed with a strain window size of 1 × 3 × 1 vectors, based on a correlation with a sub-set size of 32 voxels and 75 % overlap. At each load step, the far-field strain was computed by taking the mean of all the measured strain components, however, correlated with a coarser sub-set size of 72 voxels (75 % overlap) and post-processed with a higher strain window size of 3 × 3 × 3 vectors. The latter approach, involving considerably lower spatial resolution, was implemented to alleviate the influence of fibre breaks on the far-field strain at high UTS levels, with **Table 3** summarizing the details.

From **Fig. 10 (a)** it can be observed that, at the 950 N load step, the 'full-recovery length' averaged over eight singlets is ~63 µm. This is consistent with the SRCT estimate of 70 µm made by Scott *et al.* [14], based on the closest separation of fibre breaks along the same fibres in a T700/M21 composite. Additionally this also matches the order of magnitude of ~100 µm reported by various modelling approaches [10], [11], [12], [67]; taking into account that the distance is a function of the applied strain, local microstructure variability, fibre-matrix stiffness ratio, debond length, presence of microcracks and elastic properties of the matrix paired with inter-fibre spacing size effects [1], [10], [12], [67], [72]. A slight increase of ~7 % is observed in the 'full-recovery length' relative to the preceding load step of 900 N, with the effect being more evident on the top side of the break (right-hand side of the graph): ~1.3 µm and ~2.8 µm respectively. These measurements are consistent with those performed on singlet 'A', as illustrated in **Fig. 10 (b)**. More precisely, a 'full-recovery length' of ~67 µm is reported, coupled with a small increase from the penultimate load step, although with a reversed prominence: ~0.4 µm and ~3.3 µm on the top and bottom side of the break plane respectively. The increase in 'full-recovery length' is more obvious if the comparison is performed between the 950 N and 850 N load step: ∼1.65 µm and ∼4 µm on the top and bottom side of the break respectively. Based on singlet 'A', the maximum increase in 'full-recovery length' as returned by the DVC in the present study is ∼9 %. While the increase is not substantial, it must be viewed in the context of a strain increment of only ∼0.23 % – **Table 3**. Unpublished data based on a revised version of Swolfs' [10] model (transverse-isotropic fibre, perfectly-plastic matrix, random packing, V_f of ∼55 %) indicates that this relative increase in 'full-recovery length' agrees reasonably well with the relative increase in FEA-predicted ineffective length between similar macro-strain levels.

In terms of the underlying micromechanics, two factors are identified as potential contributors to growth in the strain transfer length with increasing applied load: (1) plastic yielding of the matrix, and (2) progressive propagation of fibre-matrix interface debonding, which both exert similar effects on the strain transfer [1], [21], [22], [23], [61], [62], [63], [64]. This is supported by the sharper gradients at the break plane associated with a higher load, which suggests that local damage is evolving. In turn, debonding is controlled by parameters such as the interfacial shear strength and/or the interface toughness, the fibre-matrix friction, the matrix yield strength and the fibre stiffness [1]. Ongoing work will aim to establish a comparison between the DVC and model predictions, highlighting the effect of various local damage modes.

Although a consistent effect is discerned, indicating that that the 'full-recovery length' increases with the applied load, the relatively small changes combined with the spatial resolution limitations and the small number of fibres investigated imply that the results should be viewed as indicative at present, rather than statistically significant. More measurements, with more broken fibres and over a wider range of load levels and a detailed comparison with micromechanical models will help clarify this matter. In contrast, the general magnitude of the 'full-recovery length' measurement is less affected by these limitations, and thus may be viewed as being a reliable conclusion.

3.3. Strain field assessment at clusters of breaks

The strain field assessment at a cluster of breaks is particularly challenging due to the 3D interaction of strain fields associated with each break (*i.e.* intersection of ineffective and overload length respectively [73]). Thus, information with minimal spatial resolution artefacts can only be retrieved from fibre breaks that form close-cluster configurations. One such example is the case of co-planar duplets, defined here as two interacting breaks with a separation of less than one fibre diameter longitudinally and two fibre diameters radially. Furthermore, given that the matrix deformation dominates the DVC output, it is not possible to reliably quantify the SCFs for the intact fibres. For consistency, correlation and post-processing parameters were retained as in the assessment of single fibre breaks (*i.e.* sub-set size of 32 voxels and 75 % overlap, with a strain window size of 1 × 3 × 1 vectors).

3.3.1. Evolution of clusters of breaks

The evolution of a ‘proto-break’ site into a singlet, and later into a cluster of breaks, is shown in **Fig. 11**. The initial fractured fibre ‘I’ in DVC slice ‘Z=36’ formed in the penultimate load step of 900 N, with fibre break ‘J’ forming in a neighbouring fibre in the final load step at 950 N, forming duplet ‘IJ’. Based on the previous work of Swolfs *et al.* [13] and Scott *et al.* [14], this incremental formation of a cluster is noted to be unusual, with break clusters much more commonly forming in a ‘burst’ as a singular event. This may be attributed to the somewhat smaller load increments being applied closer to failure (**Section 2.2.**) than in [13] and [14], allowing for a more progressive formation of clusters to be captured.

It would appear that the initial break may be triggered by a region of higher strain compared to the immediate surroundings – **Fig. 11 (a)** and **(b)**. However, it is beyond the scope of the present work to evaluate whether this state of strain is responsible (even in part) for initiating breaks. As such, considering that the carbon-fibre tensile strength distributions follow a Weibull probabilistic model, it may be assumed for the time being that singlet ‘I’ is simply a stochastic event within the material bulk. In contrast, the second fibre break ‘J’ appears to form as the result of the increased strain in the fibres surrounding the existing break. Following the development of duplet ‘IJ’ at the ultimate load step of 950 N, the local strain concentration intensifies. This increases the strain in the surrounding intact fibres, with two additional fibres of interest ‘K’ and ‘L’ failing in the same load increment – forming a second duplet ‘KL’. The residual strain from the new duplet can be visualised in **Fig. 11 (c)**, with its corresponding DVC slice ‘Z=38’ being detailed in the following section, as part of **Fig. 11 (d)**.

Including both duplets within a single ‘full-recovery length’, following the approach described in **Section 3.3.2.**, the formation of a singlet (at 900 N) in this specific cluster configuration (at 950 N) results in a recovery distance increase of ~11 % for an incremental strain of ~0.12 % – **Table 3**. This growth in ‘full-recovery length’ is greater than the ~7 % average for the eight singlets evaluated between the same load steps – **Fig. 10 (a)**.

These observations suggest that the formation of this cluster is affected by the interaction with the existing break, and its strain field. A further redistribution of strain occurs, causing a further reduction in load carrying capacity at the cluster site. In turn, the additional volume of affected material around the two breaks causes an increase in the full-recovery length when compared to single fibre fractures.

3.3.2. Effect of clusters of breaks on strain transfer lengths

Fig. 11 (c) and (d) highlight a sequence of DVC slices centred on two co-planar duplets (‘IJ’ and ‘KL’) at the 950 N load step. The first cluster is observable in slice ‘Z=36’, while the second in ‘Z=38’. The corresponding longitudinal (Y), transverse (X) and out-of-plane (Z) separation distances between the two clusters are ~21 μm, ~16 μm and ~10 μm respectively. An additional fibre break exists ~36 μm below duplet

‘IJ’ in slice ‘Z=35’, however, it is disregarded from the following analysis given its greater separation from the pair of duplets.

As in the case of single fibre breaks, the DVC output yields two near-symmetrical and distinct strain regions – an ‘elevated’ and ‘lower strain length’ respectively, on each side of the corresponding duplets. However, due to the spatial proximity of the two duplets, interaction between the strain fields now takes place, with two separate effects observable in **Fig. 11 (c)** and **(d)**: (1) a merging of the ‘lower strain lengths’, and (2) a coupling of the ‘elevated strain length’ with the ‘lower strain length’. At the presently attainable spatial resolutions, the former effect leads to an extension of the ‘full-recovery length’, while the latter promotes a dampening of the strain gradients. More precisely, these redistribution effects are a consequence of the relatively small axial separation of the duplets, with the two breaks associated with duplet ‘IJ’ being located marginally within the ‘recovery length’ of ‘KL’ and *vice versa*. This effect is consistent with that observed numerically in [73], whereby fibre breaks have been shown to trigger an SCF peak within the recovery region of other broken fibres, ultimately resulting in shorter ineffective lengths.

Fig. 12 presents the strain distributions relative to breaks ‘I’ and ‘K’, which yields two longitudinal axes from the peak strains. To account for the interaction of the strain fields, ‘IJ’ was taken as the datum. First it can be observed that the maximum strain of ∼8.8 % recorded at duplet ‘IJ’ is lower by a factor of ∼1.6 with respect to duplet ‘KL’, where a peak value of ∼5.4 % is measured. Given that the ‘KL’ strain profile is significantly dampened, the discrepancy at the fracture planes may be attributed to different damage mechanisms at the two clusters. In the absence of dissimilar damage scenarios at the fracture plane, similar peak levels would be expected within the ‘elevated strain lengths’, owing to similar cluster configurations and redistribution effects. For example, at the bottom of break ‘J’ a small feature which resembles a crack tip, or tear, is visible in between it and the neighbouring intact fibre. Although not observable here, a similar feature exists at top of break ‘J’ in an adjacent slice. Neither feature is traceable in the previous load steps. The presence of a microcrack would explain the higher strain and strain gradient captured at duplet ‘IJ’. Likewise, Swolfs *et al.* [13], predict very high strains and gradients originating at the tip of microcracks in the matrix. Secondly, the peak strain recorded at duplet ‘KL’ is not substantially higher than the average value of ∼5.15 % at the eight singlets at the equivalent load step – **Fig. 10 (a)**. This suggests that this cluster is somehow associated with less local damage at the fracture plane, making the relationship between the number of broken fibres and local microstructural damage less straightforward.

The distance over which the far-field strain is recovered from the two duplets is more difficult to interpret due to the interacting strain fields; an effect also visible through the intersecting gradients in **Fig. 12**. As such it is not possible to completely decouple the ‘full-recovery lengths’ associated with the two duplets, even more so for the four component fibre breaks. Therefore, the ‘full-recovery length’ is given by the maximum distance of ∼78 μm which encompasses both clusters. Compared to the average length of ∼63 μm recorded from **Fig. 10**

(a) at the 950 N load step, this is ~24 % higher. Interestingly, the 'full-recovery length' does not appear to increase proportionally with the effective diameter of the cluster. For example, it might be expected that if there was scaling with the linear dimensions, a doubling in the number of fibres involved in a cluster, representing a doubling in the cross-sectional area, would represent a √2 (41 %) increase in effecting cluster diameter, and a similar increase in the dimensions of all associated damage and strain fields (*e.g.* the Kelly-Tyson perfect-plasticity model [74]). Clearly such an increase is not observed in the present DVC study, which could either be due to a limitation of the technique or indicate a more complex states of damage and strain (*e.g.* as in [73]).

The DVC measured strain field at a cluster of breaks therefore indicates a state whereby the full-recovery length near fibre-breaks grows not only with the applied load, but also with cluster size. Compared to single fibre fractures, an additional layer of strain redistribution complexity is detected, and in certain cases links with higher local damage can be made. These findings can also be used to arbitrate between different modelling approaches, as for example, the model proposed by Pimenta and Pinho [75], [76] is the only one in the recent benchmarking exercise [77] that considers a growing ineffective length with applied stress and number of fibres broken in a cluster (also noted in [78]).

4. Summary and conclusions

Digital Volume Correlation was applied in conjunction with *in situ* Synchrotron Radiation Computed Tomography to investigate the strain fields at fibre breaks in unidirectional Carbon-Fibre Reinforced Polymers subjected to quasi-static tensile loading. For the material systems utilized, measurement sensitivity and noise were considered, along with the spatial filtering intrinsic to DVC strain measurements. Correlation between breaks and corresponding strain regions have been established at a level well above the measured noise. To the best of the authors' knowledge, this is the first time that 3D strain measurements have been made within the bulk of representative composite materials under applied tensile load.

To eliminate the issue associated with poor correlation along the fibre direction, the matrix was doped with a sparse population of highly contrasted sub-micrometre particles. These acted as fiducial markers, and significantly lowered the measurement uncertainty, allowing for strains to be interpreted at fibre-level. Rigid body displacement tests also confirmed that specimen translation parallel to the fibre direction is in line with the applied displacements, obviating a key problem in applying DVC to such uniformly aligned microstructures. Compared to volume images acquired through Micro-focus Computed Tomography, the metrological performance of the DVC technique was demonstrated to be superior. Furthermore, hold-at-load artefacts were mitigated due to scan times on the order of ~seconds as opposed to ~hours.

The strain field assessment at single fibre breaks resulted in 'full-recovery lengths' consistent with values reported in the modelling literature, ~50-100 µm. However, due to the spatial resolution limitations and associated DVC averaging effects, the deformation at a constituent level could not be separated (*i.e.* between fibre and matrix). Consequently, each of the ‘recovery length’ profiles encompassed an ‘elevated strain length’ associated primarily with the matrix deformation at the crack plane, followed by a ‘lower strain length’ where the DVC is expected to be a good estimate of both fibre and matrix deformation. Additionally, the ‘full-recovery lengths’ were observed to increase with the applied load, consistent with micromechanical modelling predictions in the literature, indicating that the level of microstructural damage (matrix yielding or debonding) advances with increasing load. The changes are, however, small and must be viewed in the context of a small stress range over which observations can be made, owing to the fact that fibre breaks develop exponentially with stress, with the majority of breaks occurring immediately prior to failure.

The evolution of single fibre breaks into duplets resulted in a considerably larger ‘full-recovery length’, together with an increased growth compared to single fibre breaks. To determine the relationship more accurately between the number of breaks in a cluster, and the surrounding microstructural damage, acquisition methods capable of substantially higher voxel resolution levels would have to be utilized.

This paper is consistent with the philosophy of ‘data rich mechanics’, whereby very high levels of utilisation of data obtained from individual experiments can be used to inform model development and validation. As such it represents the first step towards the overall aim of the study, which consists of a comparison between numerical and analytical model predictions. Nonetheless, the approach is not simple or direct. That is because any comparison/validation of corresponding modelling must include equivalent spatial filtering (*e.g.* sub-set grid spacing) to match the experimental constraints.

The materials and methods are now developed, and with a high level of confidence in the basic measurements, other application areas can be envisaged where microstructural influence may be important: influences of porosity or ply drops on local load paths/partitioning, compression/microbuckling, and materials with multiaxial or discontinuous reinforcement.

Acknowledgements

The research leading to these results has been conducted within the framework of the FiBreMoD project and has received funding from the European Union’s Horizon 2020 research and innovation programme under the Marie Skłodowska-Curie grant agreement No. 722626.

The authors would like to acknowledge the European Synchrotron Radiation Facility (ESRF) for provision of synchrotron radiation facilities and would like to thank Dr. Lukas Helfen and Ms. Elodie Boller for assistance in using beamline ID19. The authors recognize LaVision GmbH for the off-site software supply and technical support from Dr. David Hollis, Dr. Alex Nila and Dr. Manuel Grewer. Accompanying acknowledgement is given to Dr. Richard Boardman, Dr. Kathryn Rankin, Dr. Orestis Katsamenis and Mr. Nicholas Hale from the μ-VIS X-Ray Imaging Centre at the University of Southampton. Mr. Sebastian Rosini and Mr. Stephen Wilby from the Engineering Materials Group at the University of Southampton are also credited with assistance during the experimental campaign. Credit is further extended to Mr. Simon Beever – University of Southampton Engineering Design and Manufacturing Centre (EDMC) and Mr. Adrian Walker – Safire Associates UK for the short notice water-jet cutting of various components required for the experimental work.

Appendix A – Static noise test

Under ideal conditions, the obtained displacement vector data and the resulting calculated strains, should be equal to zero. Noise arising from the imaging system (*e.g.* photon counting statistics, electrical noise, scattered radiation) and the surrounding environment (*e.g.* induced vibrations, thermal changes) represents the most significant non-ideality, and consequently erroneous sub-set displacements will generate false strains within the results [30], [35], [40]. However, due to the novelty of the DVC technique, as yet there is no agreed standard for the assessment of the strain error (usually referred to as the strain resolution) [24], [36], [40]. For example, one approach reports the maximum standard deviation of a given strain map (plane of sub-sets) [30], [35], while a second returns the standard deviation of the measured strain components within the volume [24], [40]. Following the first approach, however, can result in overestimating the error, as results can be affected by unrepresentative localised scanning artefacts (*e.g.* rings, detector 'zingers'). In this work, the latter approach is taken for which the error is seen to form a normal distribution with a mean of ~zero. The advantage of this approach is that both the stochastic noise in the imaging system and any biases in the correlation algorithm are captured and accounted for [24], [40].

A typical effect of the sub-set size on the strain resolution is presented in **Fig. 13**. As previously reported in the literature, a compromise can be achieved between strain and spatial resolution [24], [29], [30], [32], [37], [40]. Of particular interest in this paper is the normal strain ε_{yy}, parallel to the fibre direction. Considering the normal components of the strain tensor, it can be observed that the lowest error is generally achieved in the fibre direction (Y), despite the fact that correlation along the fibres themselves has the lowest values, particularly in particle-free CFRPs [40]. This may be rationalised, as the deposition of $BaTiO_3$ during the drum winding process occurred parallel to the fibre direction as the tow was drawn through the die; essentially creating longitudinal bands of fiducial markers in the Y-direction which assists the correlation process significantly, eliminating the self-similar microstructure. Albeit for reduced spatial resolutions, a similar effect is also observed by using µCT on the particle-adapted material in [24], demonstrating reasonable consistency between the different imaging methods.

The compromise between strain and spatial resolution is a critical decision; a smaller sub-set size will contain too few unique features, in this case, the $BaTiO_3$ particles. In contrast, a larger sub-set will compromise spatial resolution [79], as the underlying deformation is representative of the average displacement of all the voxels contained within the sub-set [24], [40]. A larger sub-set size also implies a larger characteristic length for the VSG, which in turn has a negative impact on the global length-scale over which the strains are computed. As the fiducial markers are the main features used for correlating sub-sets between the different deformation states it may be assumed that matrix deformation dominates the DVC output [24].

A trade-off is identifiable in **Fig. 13** at an isotropic sub-set size of 72 voxels, where the corresponding length of the VSG measures 108 voxels. In contrast, a 32 voxel sub-set size was considered the smallest sub-set size achievable at present for reliable measurements using this material, with the lower limit being a consequence of insufficient $BaTiO_3$ particles captured by smaller sub-sets; containing less than ~10 particles per sub-set. The equivalent VSGs (for different sub-set sizes applied) are shown in **Fig. 14**, alongside the strain resolution (ε_{yy}) related to the static noise test. From **Equation 1**, it can be observed that for the particular case of a 75 % sub-set overlap, the characteristic length of the VSG measures the constituent sub-set dimension plus one half.

Appendix B – Rigid body displacement

The displacement field following a movement parallel to the fibre direction was initially computed at a sub-set size of 72 voxels (75 % overlap). The measured variation in displacement via DVC is relatively small, with an average displacement reading of 4.828 µm and a standard deviation of 0.009 µm. The induced Y-displacement was manually confirmed to the nearest pixel in Fiji ImageJ [80]; multiple measurements were taken by determining the distance between a unique feature (*e.g.* a void or $BaTiO_3$ particle) and a reference point. The manual (average) measurement indicates a displacement of ~4.55 ± 0.65 µm, which is within the accuracy of the DVC. As the present work is exclusively focused on fibre direction strain measurements, rigid body displacement analyses were only carried out in the longitudinal direction. Although not an objective here, it is acknowledged that in order to perform reliable transverse (X-direction), and out-of-plane (Z-direction) strain measurements additional noise assessment studies would be required (*e.g.* as in [40]).

A strain map indicating the rigid body correction is shown in **Fig. 15**, where the magnitude of the longitudinal strain noise is shown on a map overlapped with the microstructure. For smaller sub-sets, the SNT and RBD corrected errors (ε_{yy}) are collectively summarized in **Fig. 16**. Edge-artefacts arising from volume displacements were geometrically masked prior to initiating the correlation process, measuring 600 × 8 invalid voxels (rounded to the closest integer), across each of the 600 raw data slices.

Fig. 16 (a) shows a general trend, where the RBD corrected error tends to be slightly higher than that of the SNT. This is consistent with previous studies which have shown that rigid body displacements can induce higher errors, particularly in the translation direction, due to additional errors from the interpolation biases arising from the specimen movement [24], [30], [35], [40]. Given the single-actuator configuration of the present *in situ* experiment as well as possible compliances within the loading rig, the RBD strain resolution is considered as the relevant representation of the strain error.

Despite a different DVC framework and superior SRCT voxels resolution levels (resulting in non-identical spatial filtering), the magnitude of the RBD corrected strain resolutions are reasonably consistent with those reported in [40] using particle toughened interlayer materials.

Appendix C – Effect of strain window size

The effect of strain window size on the SNT and RBD corrected scans is visible in **Fig. 17**, where the strain resolution associated with the normal strain component ε_{yy} were reprocessed using 1 × 3 × 1 vectors and 5 × 5 × 5 vectors respectively. Correlation with a sub-set size of 32 voxels and 75 % overlap was maintained throughout. The results are compared against the default strain window size of 3 × 3 × 3 vectors. **Table 4** presents the equivalent VSGs in physical units and fibre diameters respectively, based on the number of neighbouring vectors enclosed.

The strain window limited to smoothing in the fibre direction (*i.e.* 1 × 3 × 1 vectors) leads to the highest measurement uncertainty. This is expected, as a strain window size of 3 × 3 × 3 vectors or 5 × 5 × 5 vectors will reduce the available signal-to-noise ratio by averaging the results over a larger effective volume (smoothing in the fibre direction *vs.* isotopically in the material bulk).

For real deformation tests (**Section 3.2.** and **Section 3.3.**) the size of the VSG (a function of: strain window, sub-set size and overlap) should be, however, small enough so that the real amplitude of the fluctuations is fully restored. While beyond the scope of this work, a detailed analysis has shown that an excessively large VSG is susceptible to over-smoothing of the strain data, and implicit loss in information regarding the material deformation. Nonetheless, achievement of strain measurements with very fine spatial resolution is limited in practice, as reported in [24], due to experimental constraints (*e.g.* uniqueness of the material pattern at a microstructural level). Additionally, such an implementation may cause the noise floor to exceed the signal level. Therefore, a balanced signal-to-noise ratio (SNR) must be considered independently for a given sub-set size, which is in turn linked to the materials and imaging methods used.

Figures and tables

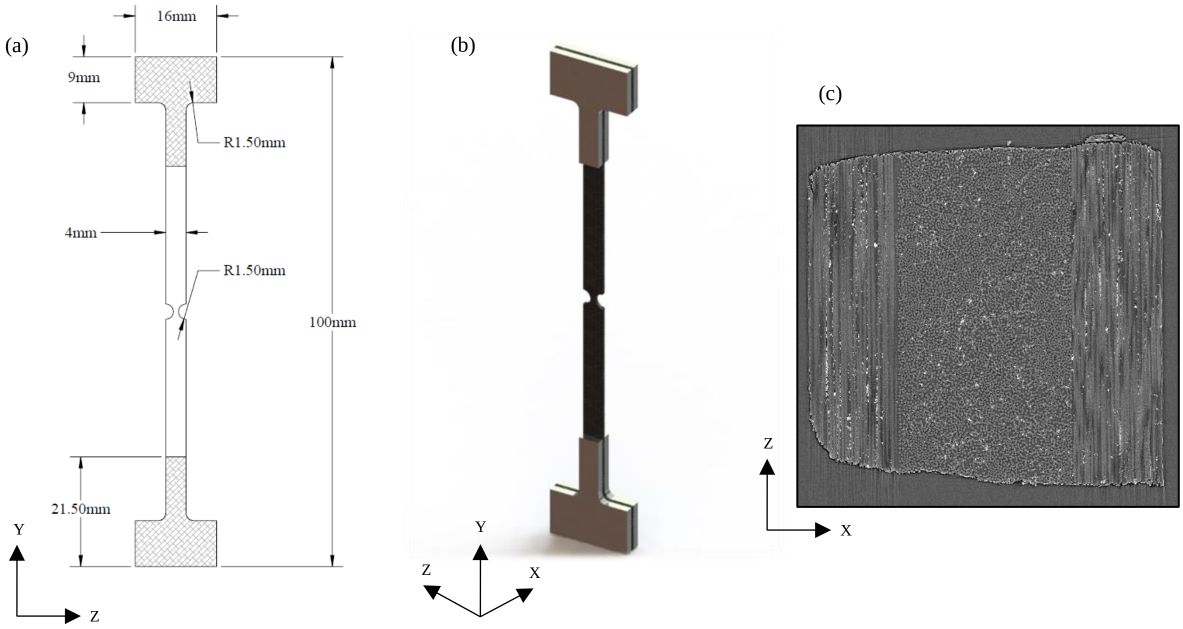

Figure 1 – Tensile specimens: (a) key specimen dimensions, (b) tabbed assembly (CFRP plus aluminium tabs), (c) SRCT slice showing a top-view of the microstructure doped with high contrast fiducial markers. Load bearing cross-sectional area of 0° plies corresponds to ~0.42 mm^2.

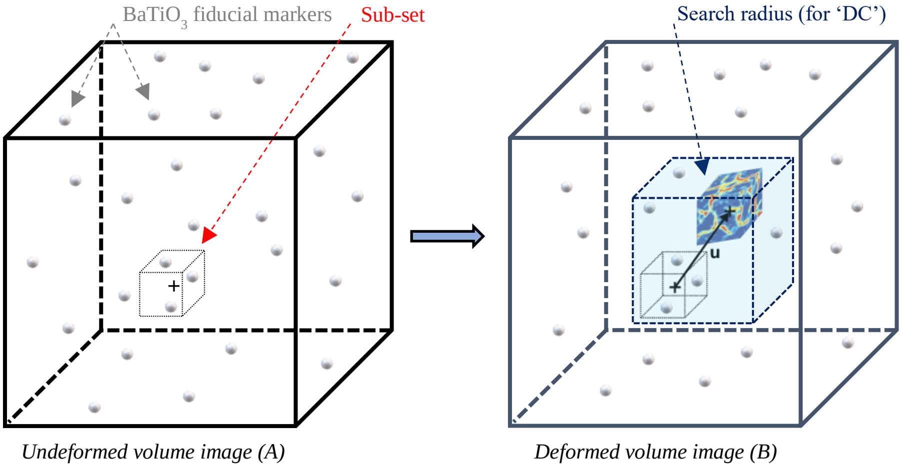

Figure 2 – Schematic diagram of the DVC process: inclusion of fiducials and presence of a user-specific search region when using the 'DC' method. Figure not to scale. Adapted from Xu [28] with permission from Elsevier and with permission from Jiroušek et al. [81].

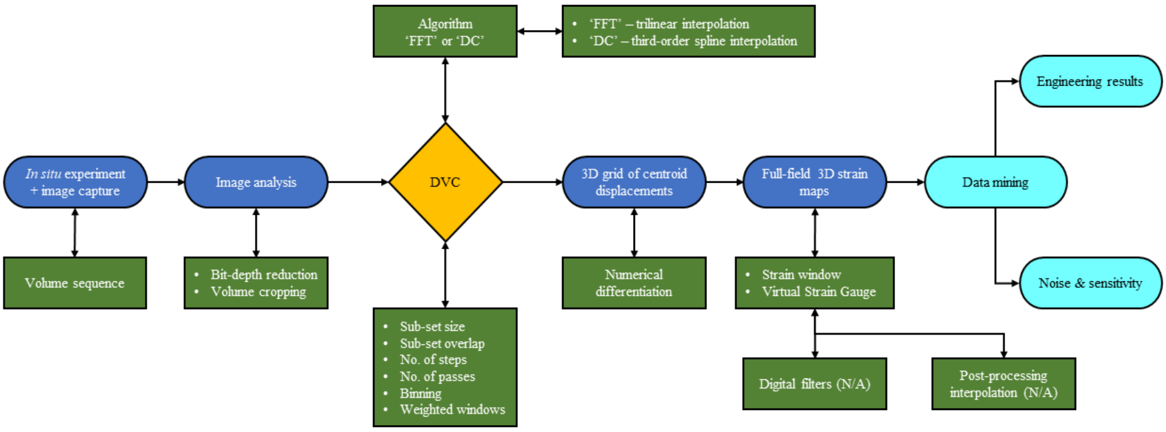

Figure 3 – Workflow diagram of the DVC process.

Final sub-set size (voxels)	FFT pre-shift (voxels)	Step 1 (voxels)	Step 2 (voxels)	Step 3 (voxels)	No. of passes steps 1-3	Voxel binning step 1	Voxel binning step 2	Voxel binning step 3
32	64	64	40	32	2	4 × 4 × 4	2 × 2 × 2	NONE
40	80	80	48	40				
48	80	80	56	48				
52	80	80	56	52				
60	96	96	64	60				
72	128	128	88	72				
80	128	128	96	80				
100	144	144	112	100				
120	176	176	136	120				

Table 1 – Summary of 'DC' settings used in the multi-step, multi-pass approach (75 % sub-set overlap). Weighted windows used in the last iteration step (dual-pass).

Sub-set size (voxels)	Step size (voxels)	No. of DVC slices (Z-direction) *	No. of raw data slices per DVC slice
32	8	75	8
52	13	46	13
60	15	40	15
72	18	33	18

*Table 2 – Number of DVC slices (planes of sub-sets) for a given sub-set size with 75 % overlap, and the corresponding number of raw data slices per DVC slice. *Nomenclature: DVC slice numbering starts with 0. Applicable to a cropped volume of 600 × 600 × 600 voxels.*

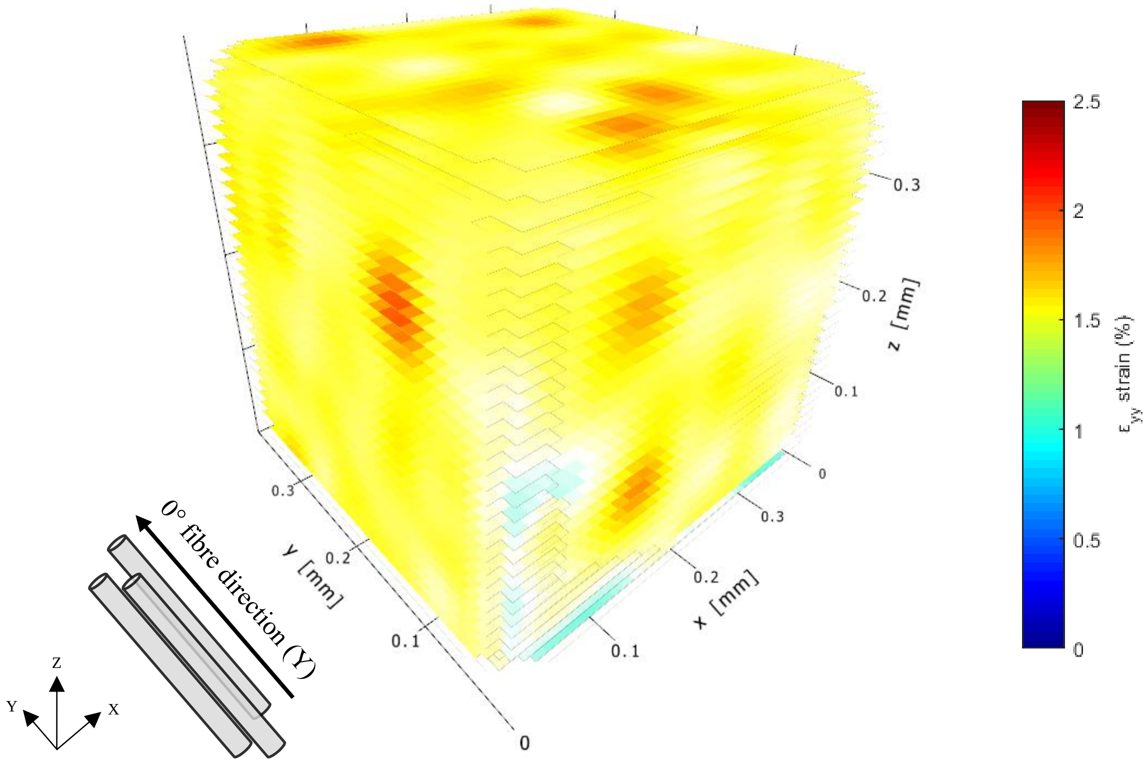

Figure 4 – Example stack comprised of 33 DVC slices in the Z-direction ('Z=0' to 'Z=32'), applicable to a sub-set size of 72 voxels with 75 % overlap, loaded to 950 N. In turn, each DVC slice (i.e. plane of sub-sets, one volumetric sub-set thick) is representative for 18 raw CT data slices. Raw data volumes cropped from the 0° plies: 600 × 600 × 600 voxels. Y-axis indicates the fibre direction. X-axis is in-plane orthogonal to the fibre direction, while the Z-axis corresponds to the out-of-plane direction.

Reference load applied (N)	Specimen UTS at applied load (%)	Load at CT acquisition (N)	DVC-based far-field strain (%) *
850	88	765	~1.25
900	93	810	~1.37
950	98	855	~1.50

*Table 3 – Far-field and recovery strain as a function of different load levels. *Strains computed at acquisition load and not compensated for existing preload in the specimen.*

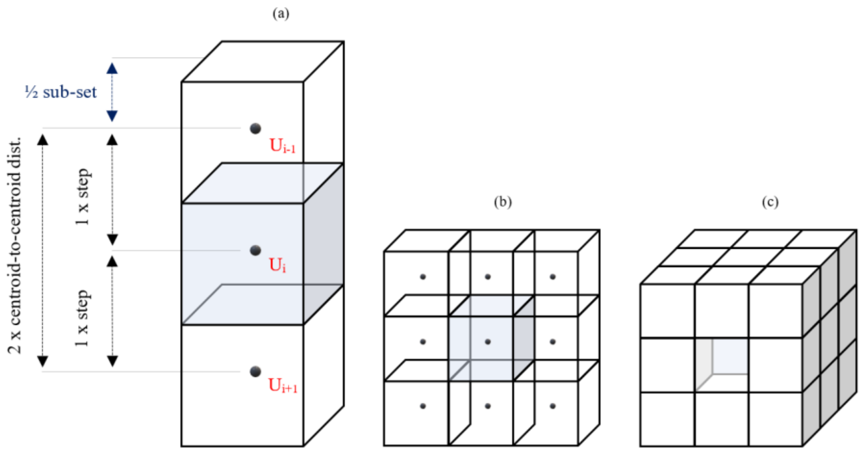

Figure 5 – Schematic illustration of different VSGs , depending on the strain window size (L_{SW}) used: (a) anisotropic – L_{SW} of 1 × 3 × 1 vectors, (b) anisotropic – L_{SW} of 3 × 3 × 1 vectors, and (c) isotropic – L_{SW} of 3 × 3 × 3 vectors. Each cube represents a sub-set and its associated centroid, with a grid spacing of one step. Sub-sets are not overlapped here for simplicity reasons. Strain window size of 1 × 3 × 1 emphasises smoothing along the fibre direction, 3 × 3 × 1 in the fibre layup plane, and 3 × 3 × 3 smooths isotopically. Higher-order strain window sizes are possible, but this can lead to an over-smoothing of the strains computed (i.e. reduction in signal-to-noise ratio).

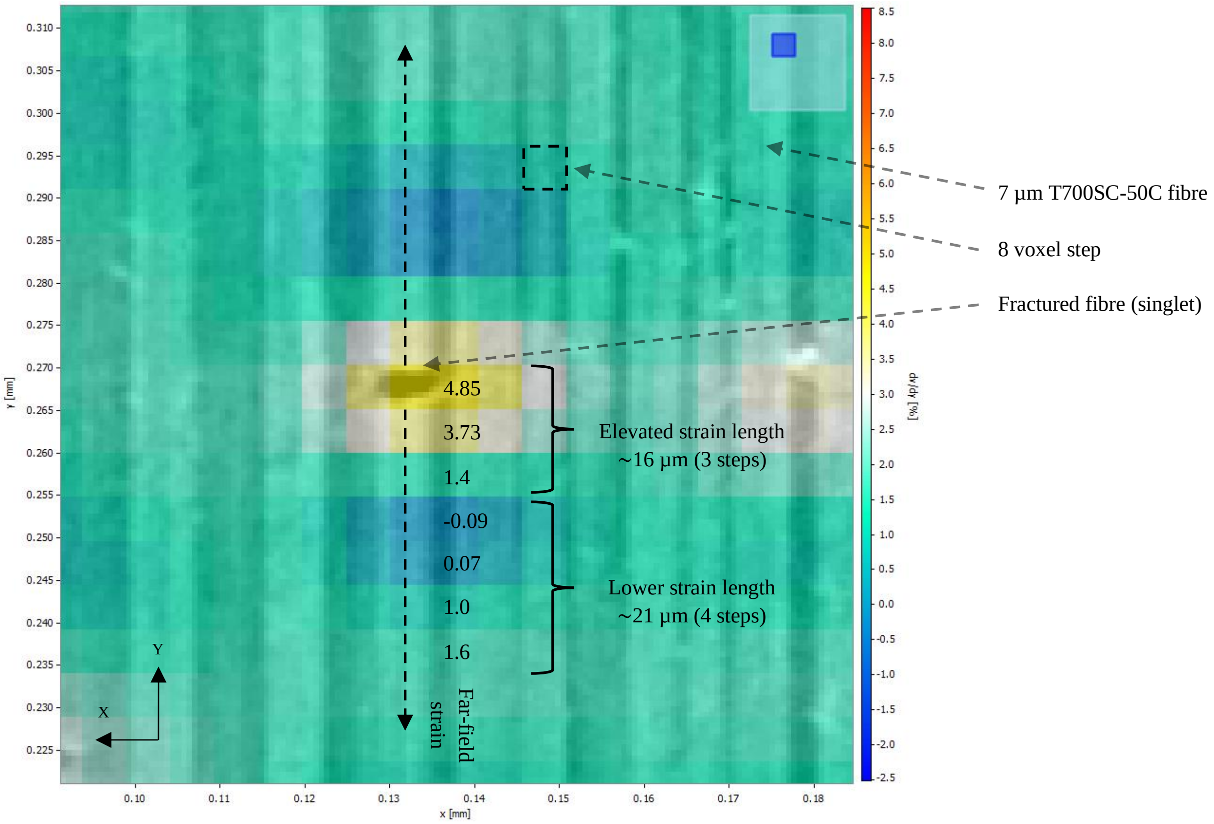

Figure 6 – DVC slice 'Z=23' illustrating the ε_{yy} strain field surrounding singlet 'C'. Following correlation with a sub-set size of 32 voxels (75 % overlap) and strain post-processing with a strain window size of 1 × 3 × 1 vectors, the DVC output yields two near-symmetrical and distinct strain regions longitudinally from the break plane: (1) an 'elevated strain length' measuring ~16 µm, and (2) a 'lower strain length' of ~21 µm, after which the far-field strain level of 1.5 % is attained. Microstructure subjected to in situ tensile loading of 950 N (~98 % UTS), with acquisition performed at 855 N. FOV amounts to ~100 µm × ~100 µm. The measurement error corresponds to ~0.093 % (see Appendices).

Fig. 7

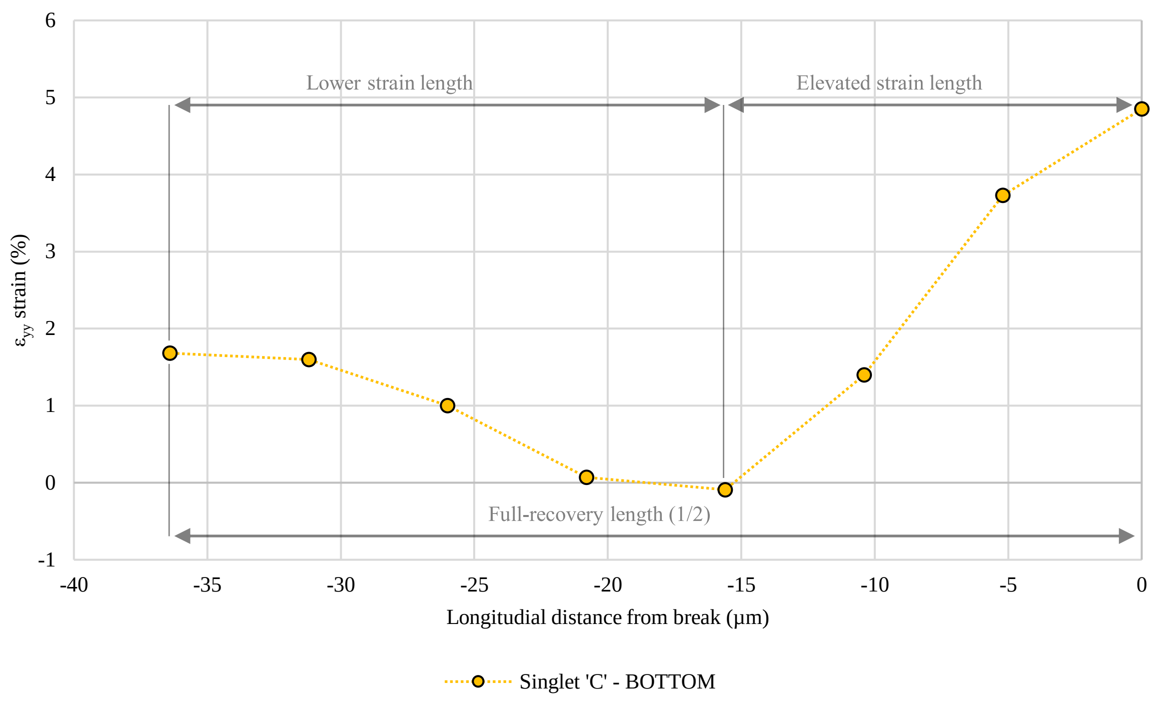

Figure 7 – Half of the 'full-recovery length' split into the two distinct strain regions, measured longitudinally from the bottom side of singlet 'C'. The measurement error corresponds to ~0.093 %.

Fig. 8

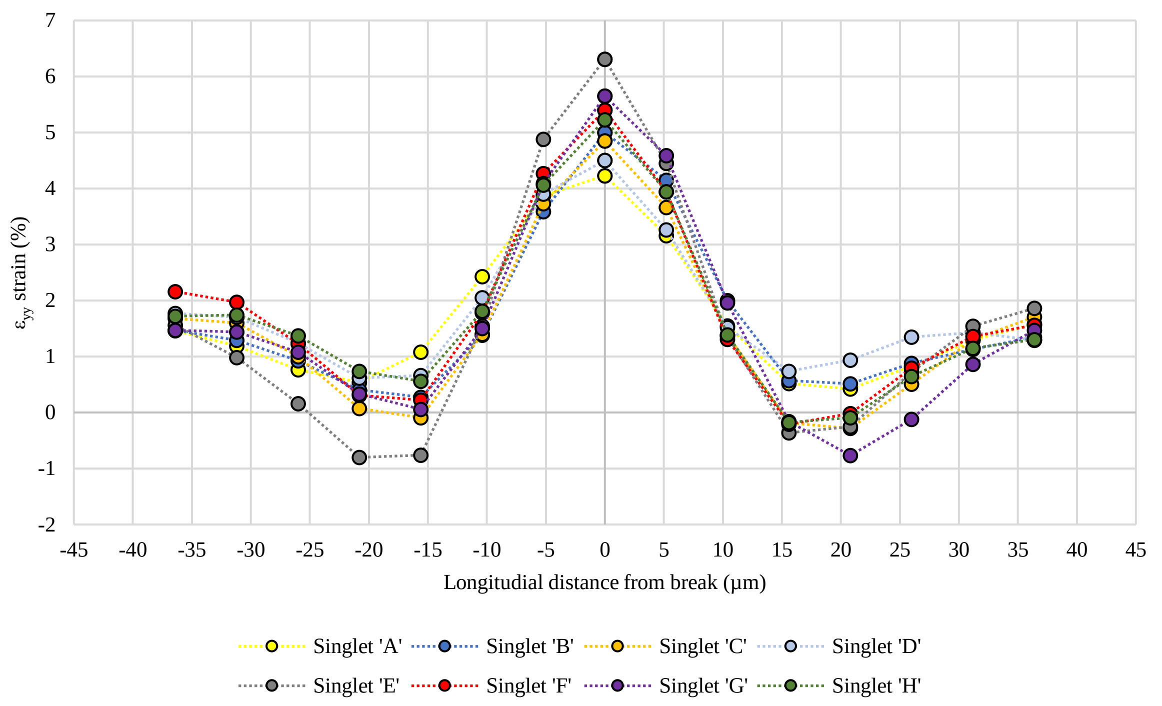

Figure 8 – Strain gradients (ε_{yy}) measured longitudinally from eight distinct singlets (both sides of the break plane). Microstructure subjected to in situ tensile loading of 950 N (~98 % UTS), with acquisition performed at 855 N. The measurement error corresponds to ~0.093 %.

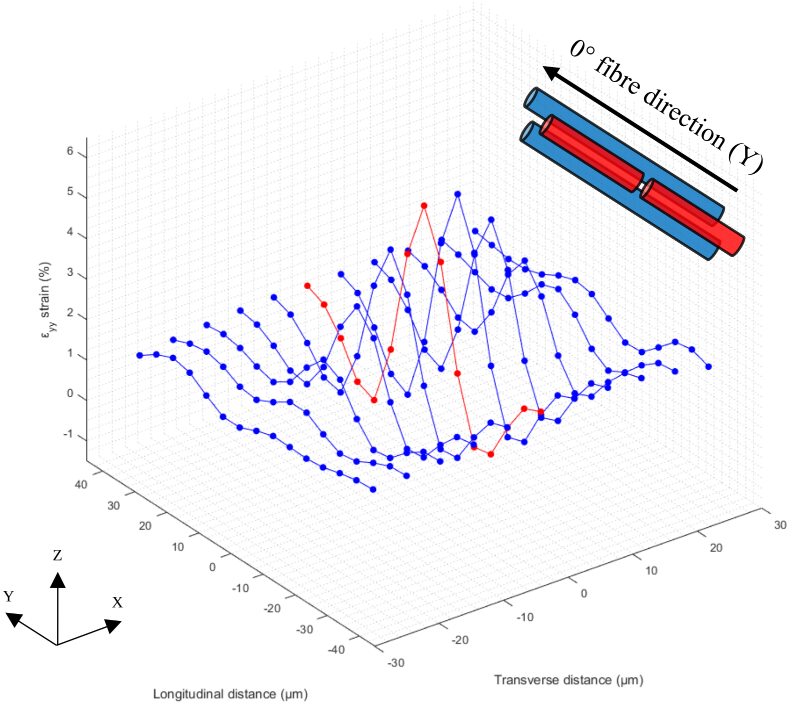

Figure 9 – Strain gradient (ε_{yy}) measured longitudinally from singlet 'F' (both sides of the break plane) and repeated stepwise in the transverse direction (X). The far-field strain level of 1.5 % is attained beyond a radial distance of ~26 μm. Strain distribution indicated in red follows a longitudinal axis from the break plane. Results applicable to DVC slice 'Z=35' Microstructure subjected to in situ tensile loading of 950 N (~98 % UTS), with acquisition performed at 855 N. The measurement error corresponds to ~0.093 %.

Fig. 10 (a)

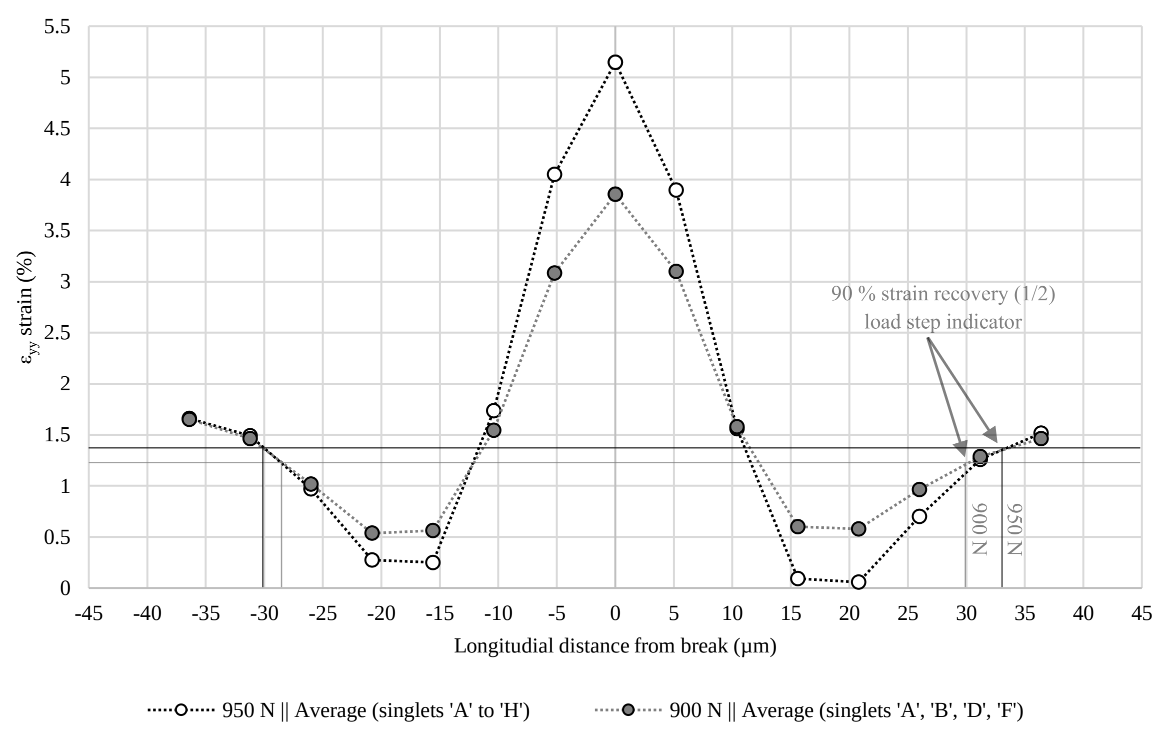

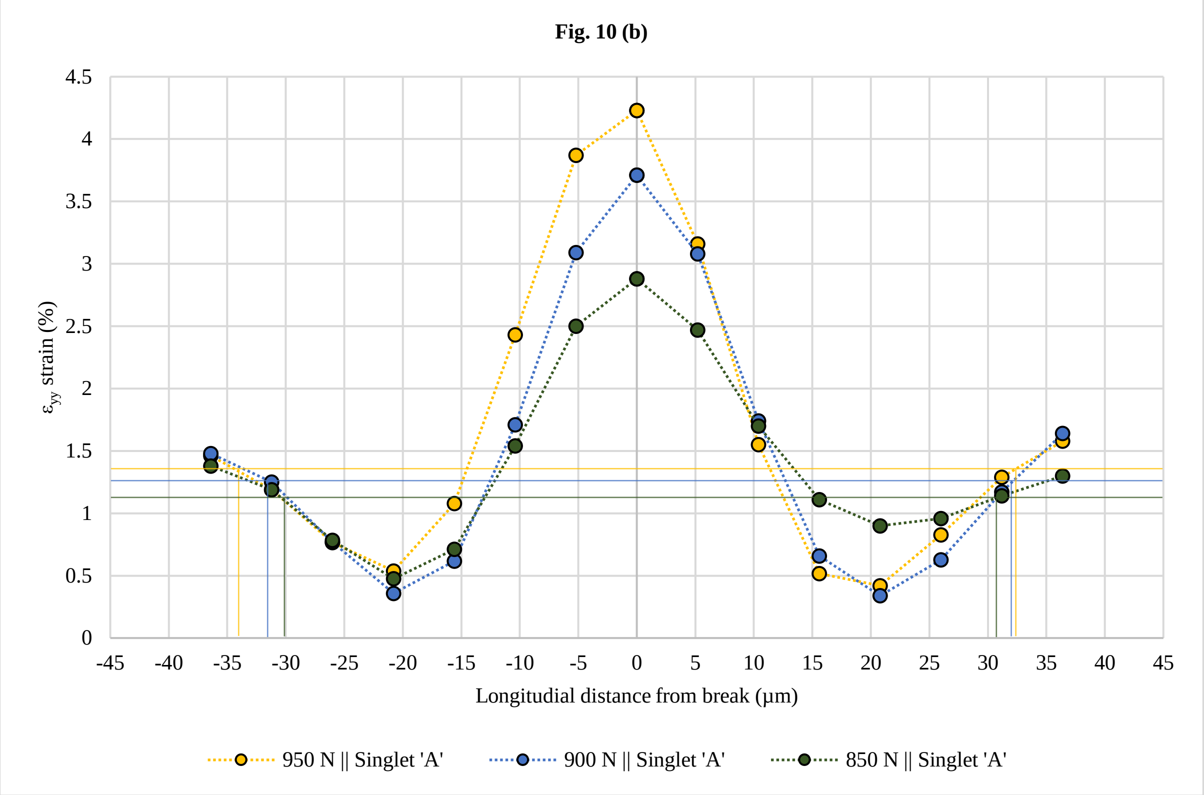

Figure 10 – Strain gradients (ε_{yy}) indicating 90 % strain recovery for the different applied load steps: (a) average of eight distinct singlets ('A' to 'H'), and (b) singlet ('A'). Measurements performed on both sides of the break plane. The measurement error corresponds to ~0.093 %.

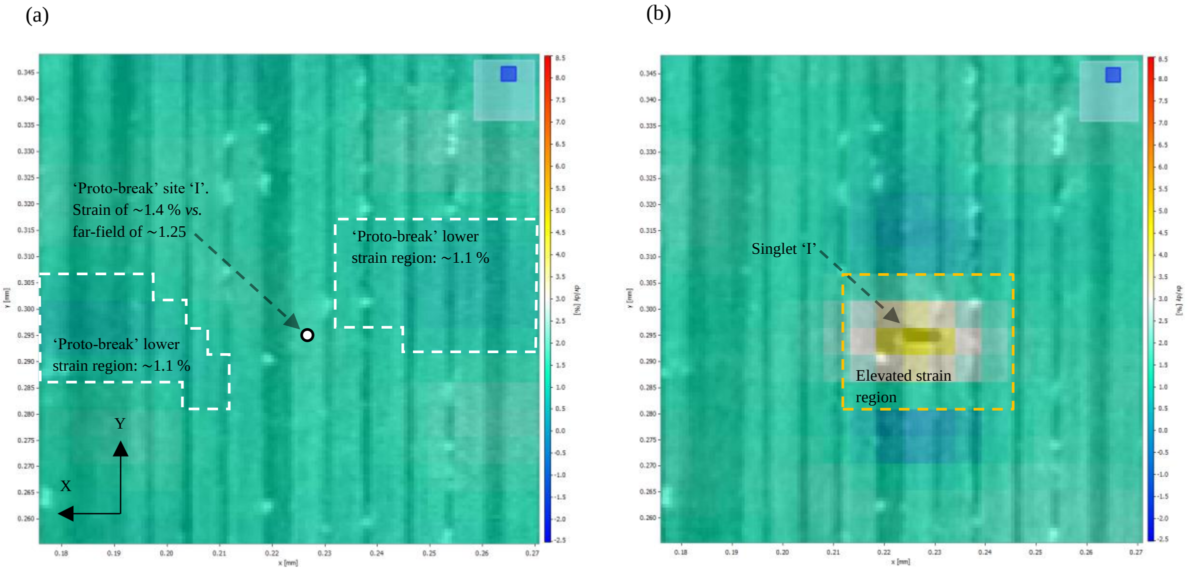

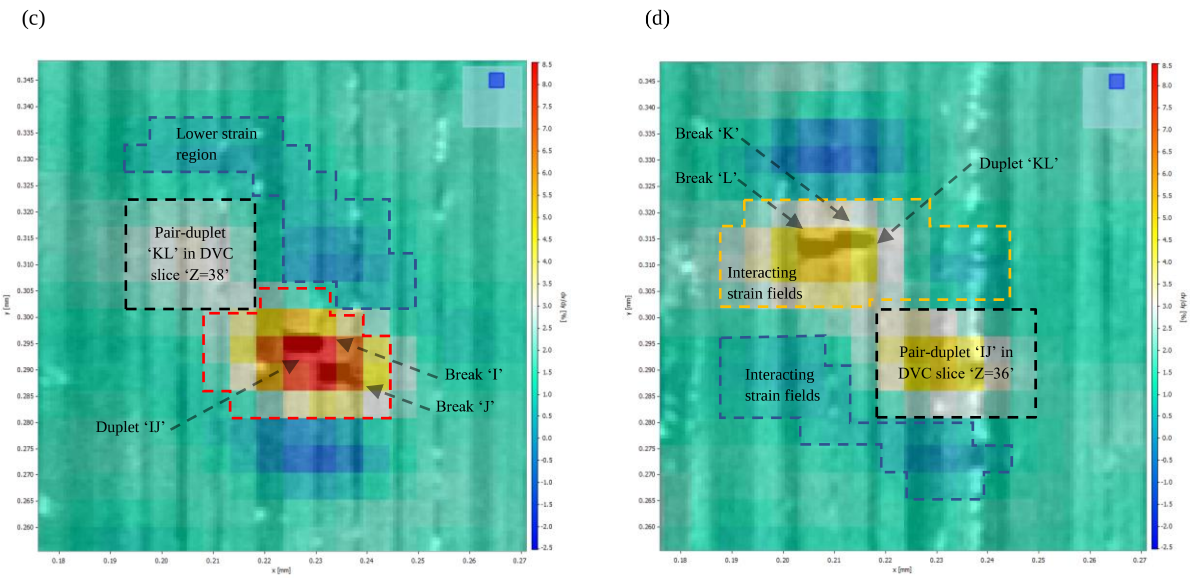
(c) (d)

Figure 11 – Illustrating the evolution of a cluster of breaks: (a) 'proto-break' site at the 850 N load step – DVC slice 'Z=36', (b) one singe break at the 900 N load step – DVC slice 'Z=36', (c) duplet 'IJ' at the 950 N load step – DVC slice 'Z=36', (d) duplet 'KL' at the 950 load step step – DVC slice 'Z=38'. Note the interacting ε_{yy} *strain fields surrounding duplets 'IJ' and 'KL' respectively. Correlation performed with a sub-set size of 32 voxels (75 % overlap), while strains were post-processed with a strain window size of 1 × 3 × 1 vectors. FOV amounts to ~100 µm × ~100 µm. The measurement error corresponds to ~0.093 %.*

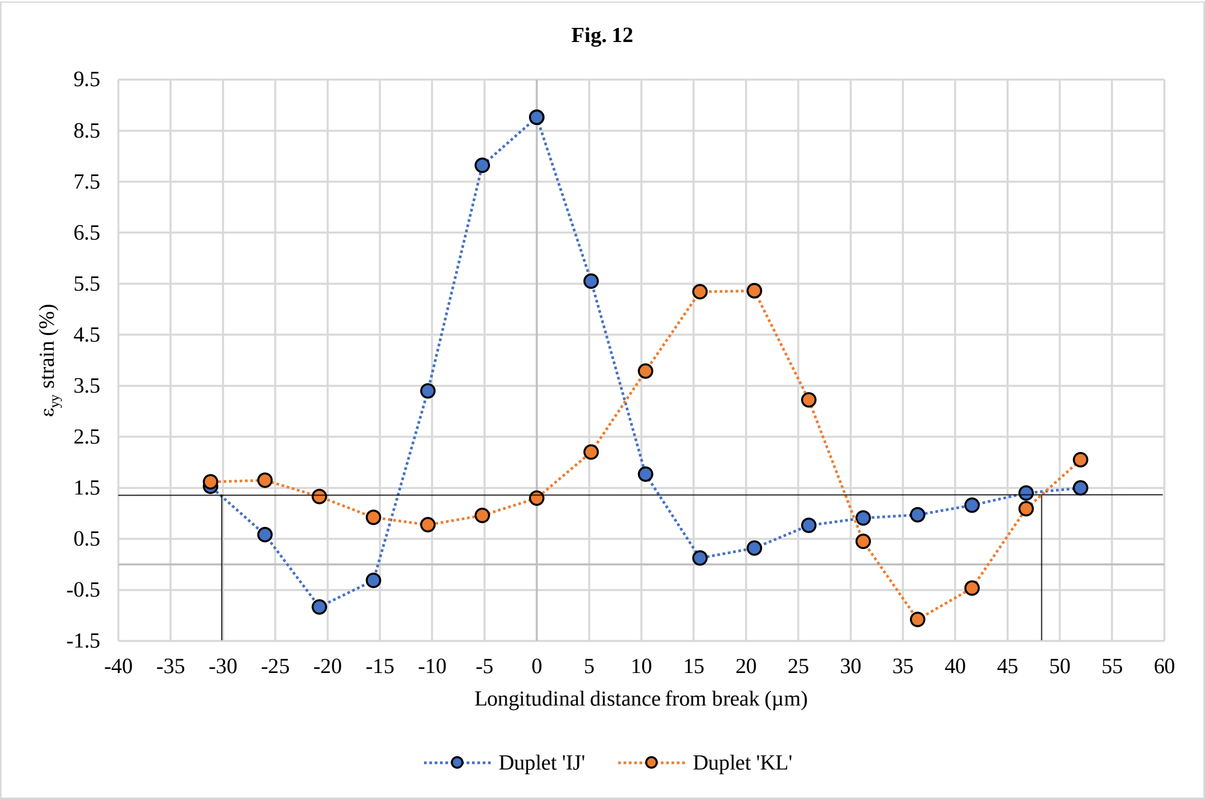

Figure 12 – Strain gradients (ε_{yy}) *measured longitudinally from breaks 'I' and 'K' of the two duplets (both sides of the break plane). Note the longitudinal (visible), transverse and out-of-plane separation distances of ~21 µm, ~16 µm and ~10 µm respectively. Microstructure subjected to in situ tensile loading of 950 N (~98 % UTS), with acquisition performed at 855 N. The measurement error corresponds to ~0.093 %.*

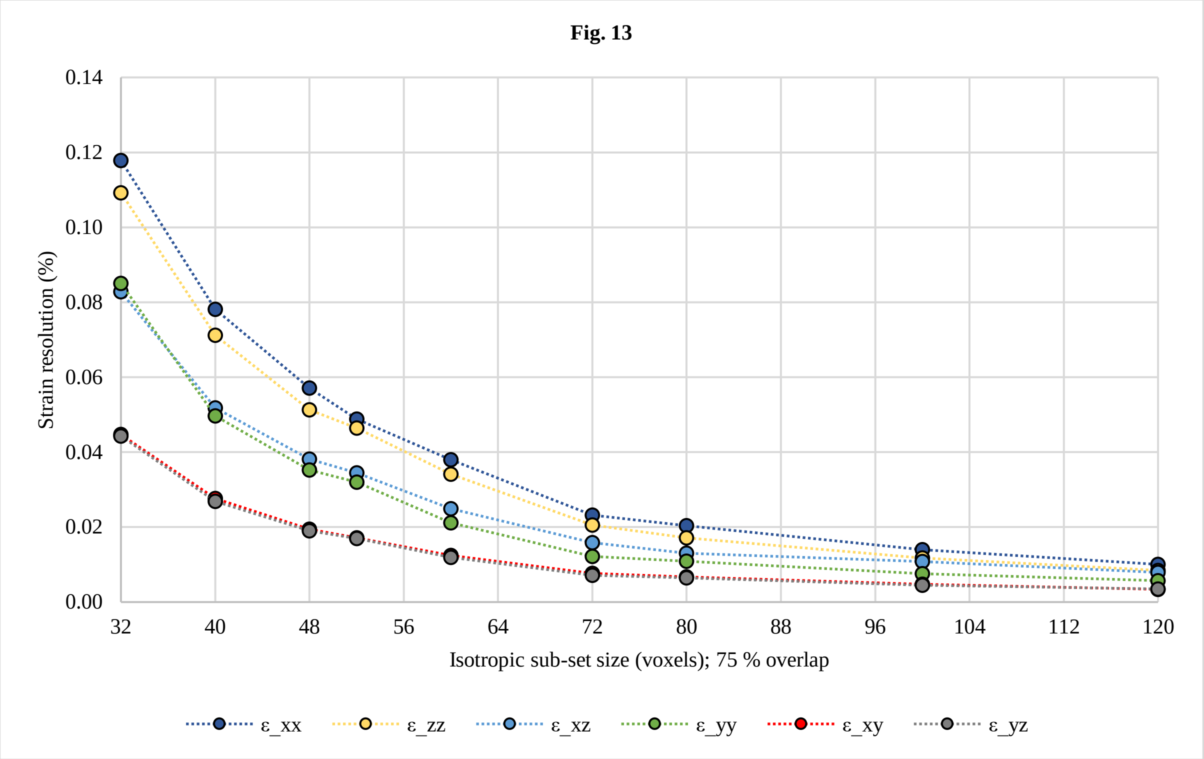

Figure 13 – The influence of sub-set size on the strain resolution during SNT scanning (expressed as the standard deviation of the measured strain values), illustrating the compromise between strain and spatial resolution. The ε_{yy} component of the strain tensor denotes the longitudinal (fibre) strain, ε_{xx} the in-plane transverse strain, while the out-of-plane strain component is given by ε_{zz}.

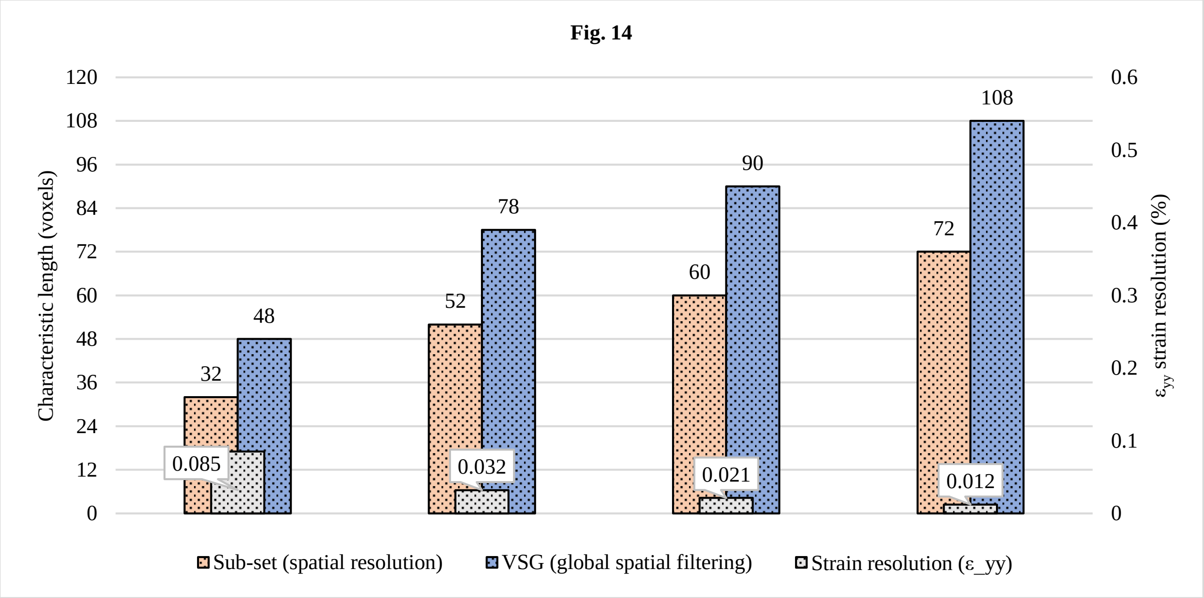

Figure 14 – Illustration of VSG and sub-set size, in conjunction with spatial resolution vs. strain resolution (ε_{yy}). Voxel size corresponds to 0.65 µm.

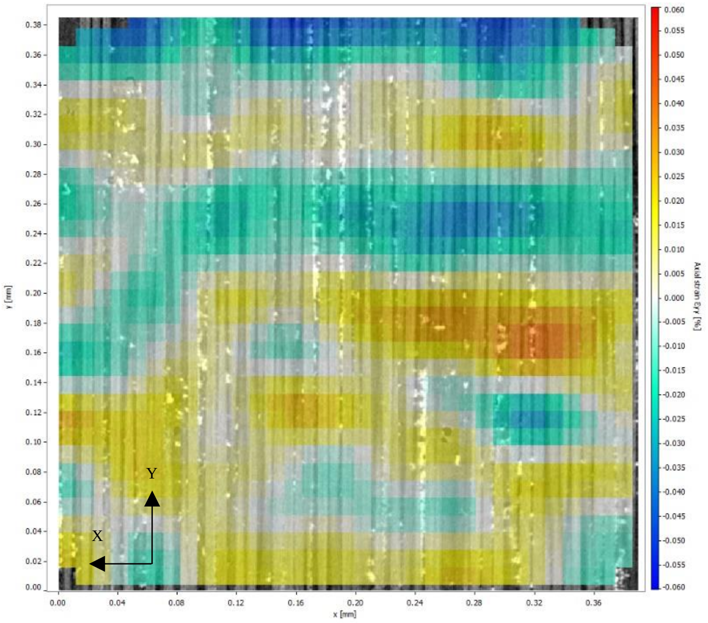

Figure 15 – DVC slice 'Z=16' illustrating the ε_{yy} strain map (noise) overlaid with the microstructure following RBD correction. Masking applied (600 × 8 × 600 voxels) to remove edge artefacts for the Y-displaced scans. Map range: -0.060 to 0.060 %. Applicable for a correlation performed with a sub-set size of 72 voxels and 75 % overlap.

Fig. 16 (a)

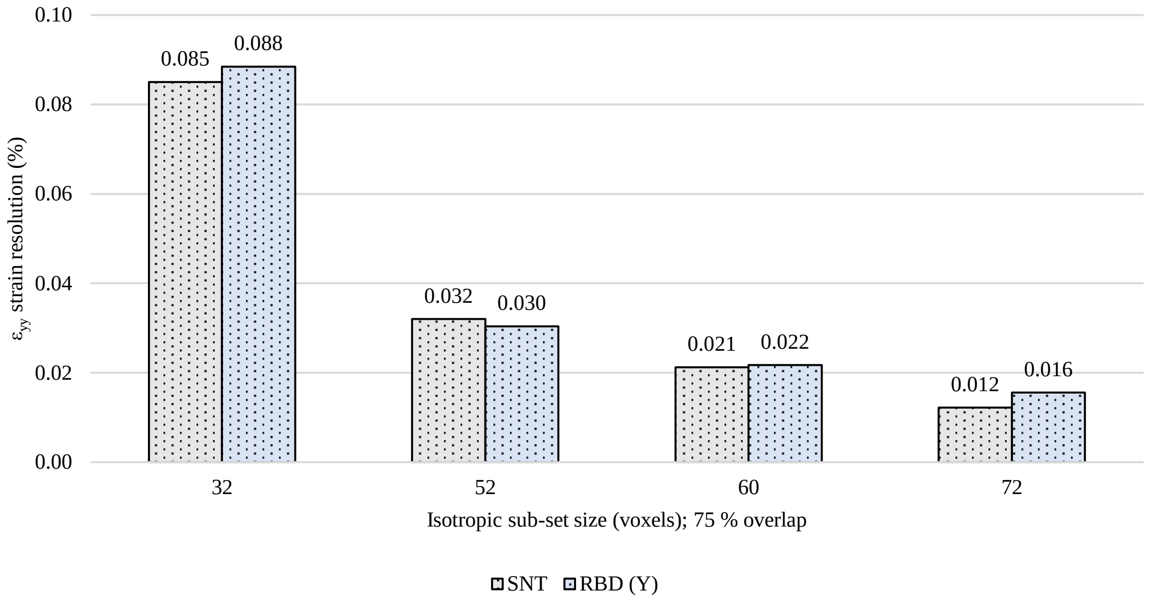

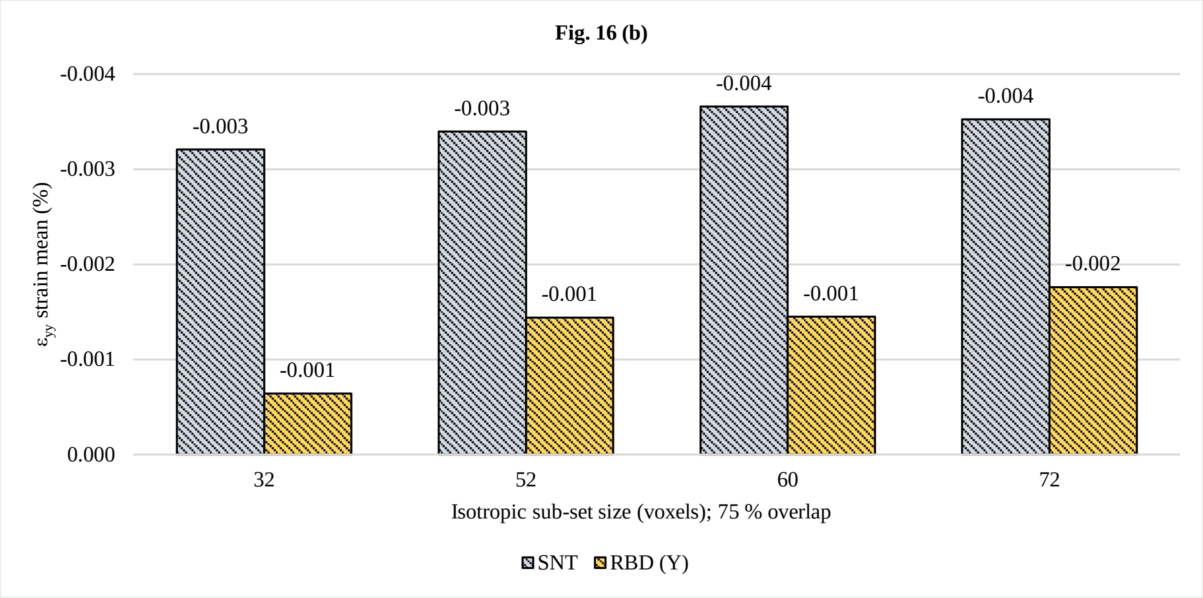

Figure 16 – (a) Strain resolution (ε_{yy}), and (b) strain mean (ε_{yy}) for the SNT and RBD corrected scans for various sub-set sizes with 75 % overlap. Masking applied (600 × 8 × 600 voxels) to remove edge artefacts for the Y-displaced scans.

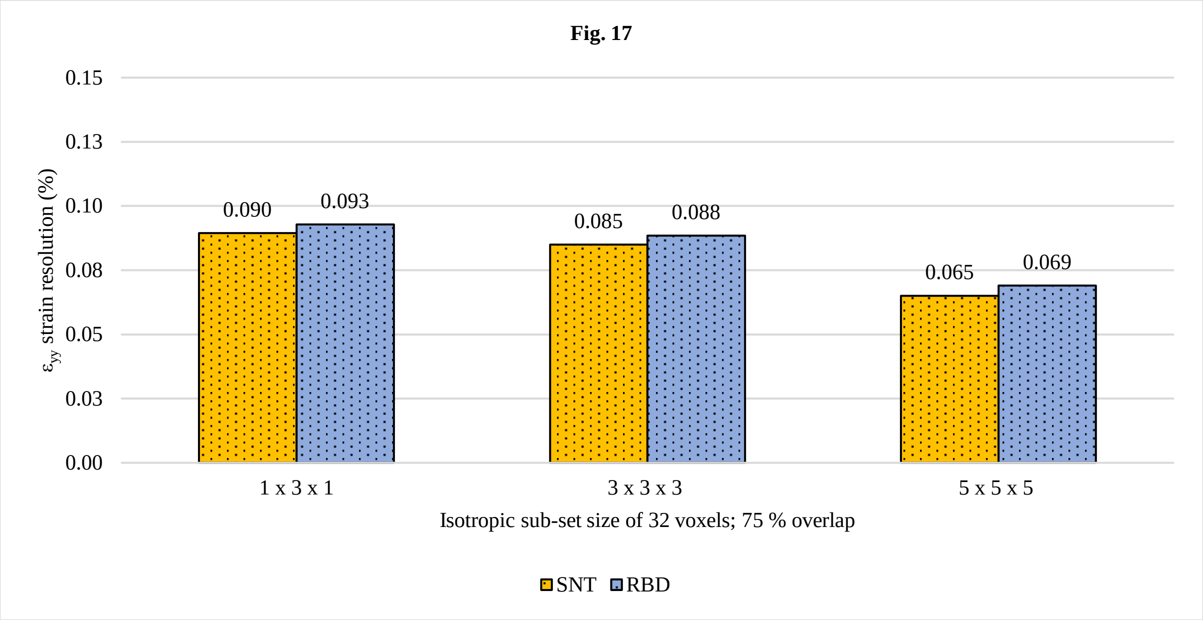

Figure 17 – Strain resolution (ε_{yy}) for the SNT and RBD corrected scans for various strain window sizes (L_{sw}), computed with a sub-set size of 32 voxels and 75 % overlap.

Strain window size (vectors)	VSG size (voxels)	VSG size (µm)	VSG size Equivalent fibre Ø (µm)
1 × 3 × 1	32 × 48 × 32	20.8 × 31.2 × 20.8	~3 × ~4.5 × ~3
3 × 3 × 3	48 × 48 × 48	31.2 × 31.2 × 31.2	~4.5 × ~4.5 × ~4.5
5 × 5 × 5	64 × 64 × 64	41.6 × 41.6 × 41.6	~6 × ~6 × ~6

Table 4 – Equivalent VSG sizes in physical units (1 voxel = 0.65 µm) and fibre diameters respectively (1 fibre diameter = 7 µm), based on different strain window sizes, applicable to a sub-set size of 32 voxels with 75 % overlap.

Bibliography

[1] Y. Swolfs, I. Verpoest and L. Gorbatikh, “A review of input data and modelling assumptions in longitudinal strength models for unidirectional fibre-reinforced composites,” *Composite Structures,* vol. 150, pp. 153-172, 2016.

[2] J. Watanabe, F. Tanaka, H. Okuda and T. Okabe, “Tensile strength distribution of carbon fibers at short gauge lengths,” *Advanced Composite Materials,* vol. 23, no. 5-6, pp. 535-550, 2014.

[3] J. M. Hedgepeth, “Stress concentrations in filamentary structures (NASA-TN-D-882, L-1502),” NASA Langley Research Center, Hampton, VA, USA, 1961.

[4] J. M. Hedgepeth and P. Van Dyke, “Local stress concentrations in imperfect filamentary composite materials,” *Journal of Composite Materials,* vol. 1, no. 3, pp. 294-309, 1967.

[5] C. Zweben, “Tensile failure of fiber composites,” *AIAA Journal,* vol. 6, no. 12, pp. 2325-2331, 1968.

[6] H. Fukuda, “Stress concentration factors in unidirectional composites with random fiber spacing,” *Composites Science and Technology,* vol. 22, no. 2, pp. 153-163, 1985.

[7] Z. Xia, W. A. Curtin and T. Okabe, “Green's function vs. shear-lag models of damage and failure in fiber composites,” *Composites Science and Technology,* vol. 62, no. 10-11, pp. 1279-1288, 2002.

[8] Z. Xia, T. Okabe and W. A. Curtin, “Shear-lag versus finite element models for stress transfer in fiber-reinforced composites,” *Composites Science and Technology,* vol. 62, no. 9, pp. 1141-1149, 2002.

[9] B. W. Rosen, “Tensile failure of fibrous composites,” *AIAA Journal,* vol. 2, no. 11, pp. 1985-1991, 1964.

[10] Y. Swolfs, L. Gorbatikh, V. Romanov, S. Orlova, S. V. Lomov and I. Verpoest, “Stress concentrations in an impregnated fibre bundle with random fibre packing,” *Composites Science and Technology,* vol. 74, pp. 113-120, 2013.

[11] M. R. Nedele and M. R. Wisnom, “Three-dimensional finite element analysis of the stress concentration at a single fibre break,” *Composites Science and Technology,* vol. 51, no. 4, pp. 517-524, 1994.

[12] M. R. Nedele and M. R. Wisnom, “Stress concentration factors around a broken fibre in a unidirectional carbon fibre-reinforced epoxy,” *Composites,* vol. 25, no. 7, pp. 549-557, 1994.

[13] Y. Swolfs, H. Morton, A. E. Scott, L. Gorbatikh, P. A. S. Reed, I. Sinclair, S. M. Spearing and I. Verpoest, “Synchrotron radiation computed tomography for experimental validation of a tensile strength model for unidirectional fibre-reinforced composites,” *Composites Part A,* vol. 77, pp. 106-113, 2015.

[14] A. E. Scott, M. N. Mavrogordato, P. Wright, I. Sinclair and S. M. Spearing, "In situ fibre fracture measurement in carbon-epoxy laminates using high resolution computed tomography," *Composites Science and Technology,* vol. 71, no. 12, pp. 1471-1477, 2011.

[15] A. E. Scott, I. Sinclair, S. M. Spearing, A. Thionnet and A. R. Bunsell, "Damage accumulation in a carbon/epoxy composite: Comparison between a multiscale model and computed tomography experimental results," *Composites Part A,* vol. 43, no. 9, pp. 1514-1522, 2012.

[16] A. Thionnet, H. Y. Chou and A. R. Bunsell, "Fibre break processes in unidirectional composites," *Composites Part A,* vol. 65, pp. 148-160, 2014.

[17] Y. Swolfs, I. Verpoest and L. Gorbatikh, "Issues in strength models for unidirectional fibre-reinforced composites related to Weibull distributions, fibre packings and boundary effects," *Composites Science and Technology,* vol. 114, pp. 42-49, 2015.

[18] S. C. Garcea, I. Sinclair, S. M. Spearing and P. J. Withers, "Mapping fibre failure in situ in carbon fibre reinforced polymers by fast synchrotron X-ray computed tomography," *Composites Science and Technology,* vol. 149, pp. 81-89, 2017.

[19] S. Rosini, M. N. Mavrogordato, O. Egorova, E. S. Matthews, S. E. Jackson, S. M. Spearing and I. Sinclair, "In situ statistical measurement of local morphology in carbon-epoxy composites using synchrotron X-ray computed tomography," *Composites Part A,* vol. 125, pp. 1-14, 2019.

[20] P. W. J. van den Heuvel, T. Peijs and R. J. Young, "Analysis of stress concentrations in multi-fibre microcomposites by means of Raman spectroscopy," *Journal of Materials Science Letters,* vol. 15, no. 21, pp. 1908-1911, 1996.

[21] P. W. J. van den Heuvel, T. Peijs and R. J. Young, "Failure phenomena in two-dimensional multi-fibre microcomposites. Part 4 – A Raman spectroscopic study on the influence of the matrix yield stress on stress concentrations," *Composites Part A,* vol. 31, no. 2, pp. 165-171, 2000.

[22] Y. Huang and R. J. Young, "Analysis of the fragmentation test for carbon-fibre/epoxy model composites by means of Raman spectroscopy," *Composites Science and Technology,* vol. 52, no. 4, pp. 505-517, 1994.

[23] Y. Huang and R. J. Young, "Interfacial behaviour in high temperature cured carbon fibre/epoxy resin model composite," *Composites,* vol. 26, no. 8, pp. 541-550, 1995.

[24] E. Schöberl, M. N. Mavrogordato, I. Sinclair and S. M. Spearing, "Fibre-direction strain measurement in a composite ply under pure bending using digital volume correlation and micro-focus computed tomography," *Manuscript accepted for publication in Journal of Composite Materials,* 2020.

[25] A. J. Moffat, P. Wright, J.-Y. Buffiere, I. Sinclair and S. M. Spearing, "Micromechanisms of damage in 0° splits in a [90/0]s composite material using synchrotron radiation computed tomography," *Scripta Materialia,* vol. 59, no. 10, pp. 1043-1046, 2008.

[26] P. Wright, A. J. Moffat, I. Sinclair and S. M. Spearing, "High resolution tomographic imaging and modelling of notch tip damage in a laminated composite," *Composites Science and Technology,* vol. 70, no. 10, pp. 1444-1452, 2010.

[27] B. Pan, K. Qian, H. Xie and A. Asundi, “Two-dimensional digital image correlation for in-plane displacement and strain measurement: a review,” *Measurement Science and Technology,* vol. 20, no. 6, pp. 1-17, 2009.

[28] F. Xu, “Quantitative characterization of deformation and damage process by digital volume correlation: A review.,” *Theoretical & Applied Mechanics Letters,* vol. 8, no. 2, pp. 83-96, 2018.

[29] M. Palanca, L. Cristofolini, E. Dall’Ara, M. Curto, F. Innocente, V. Danesi and G. Tozzi, “Digital volume correlation can be used to estimate local strains in natural and augmented vertebrae: An organ-level study,” *Journal of Biomechanics,* vol. 49, no. 16, pp. 3882-3890, 2016.

[30] F. Gillard, R. P. Boardman, M. N. Mavrogordato, D. Hollis, I. Sinclair, F. Pierron and M. Browne, “The application of Digital Volume Correlation (DVC) to study the microstructural behaviour of trabecular bone during compression,” *Journal of the Mechanical Behavior of Biomedical Materials,* vol. 29, pp. 480-499, 2014.

[31] S. P. Timoshenko, Strength of materials. Part 1 – Elementary theory and problems, 2nd ed., New York City, NY, USA: David Van Nostrand Company Inc., 1940, pp. 88-97.

[32] L. Liu and E. F. Morgan, “Accuracy and precision of digital volume correlation in quantifying displacements and strains in trabecular bone,” *Journal of Biomechanics,* vol. 40, no. 15, pp. 3516-3520, 2007.

[33] K. Madi, G. Tozzi, Q. H. Zhang, J. Tong, A. Cossey, A. Au, D. Hollis and F. Hild, “Computation of full-field displacements in a scaffold implant using digital volume correlation and finite element analysis,” *Medical Engineering & Physics,* vol. 35, no. 9, pp. 1298-1312, 2013.

[34] R. Brault, A. Germaneau, J. C. Dupré, P. Doumalin, S. Mistou and M. Fazzini, “In-situ analysis of laminated composite materials by X-ray micro-computed tomography and digital volume correlation,” *Experimental Mechanics,* vol. 53, pp. 1143-1151, 2013.

[35] F. Pierron, S. A. McDonald, D. Hollis, J. Fu, P. J. Withers and A. Alderson, “Comparison of the mechanical behaviour of standard and auxetic foams by X-ray computed tomography and digital volume correlation,” *Strain,* vol. 49, no. 6, pp. 467-482, 2013.

[36] M. Palanca, G. Tozzi, L. Cristofolini, M. Viceconti and E. Dall'Ara, “Three-dimensional local measurements of bone strain and displacement: comparison of three digital volume correlation approaches,” *Journal of Biomedical Engineering,* vol. 137, no. 7, pp. 1-14, 2015.

[37] L. Wang, N. Limodin, A. El Bartali, J.-F. Witz, R. Seghir, J.-Y. Buffiere and E. Charkaluk, “Influence of pores on crack initiation in monotonic tensile and cyclicloadings in lost foam casting A319 alloy by using 3D in-situ analysis,” *Materials Science & Engineering A,* vol. 673, pp. 362-372, 2016.

[38] D. Kytýř, P. Zlámal, P. Koudelka, T. Fíla, N. Krčmářová, I. Kumpová, D. Vavřík, A. Gantar and S. Novak, “Deformation analysis of gellan-gum based bone scaffold using on-the-fly tomography,” *Materials & Design,* vol. 134, pp. 400-417, 2017.

[39] B. Wang, B. Pan and G. Lubineau, “Morphological evolution and internal strain mapping of pomelo peel using X-ray computed tomography and digital volume correlation,” *Materials & Design,* vol. 137, pp. 305-315, 2018.

[40] G. Borstnar, F. Gillard, M. N. Mavrogordato, I. Sinclair and S. M. Spearing, “Three-dimensional deformation mapping of Mode I interlaminar crack extension in particle-toughened interlayers,” *Acta Materialia,* vol. 103, pp. 63-70, 2015.

[41] M. P. Fernández, A. H. Barber, G. W. Blunn and G. Tozzi, “Optimization of digital volume correlation computation in SR-microCT images of trabecular bone and bone-biomaterial systems,” *Journal of Microscopy,* vol. 272, no. 3, pp. 213-228, 2018.

[42] S. C. Garcea, Y. Wang and P. J. Withers, “X-ray computed tomography of polymer composites,” *Composites Science and Technology,* vol. 156, pp. 305-319, 2018.

[43] J. M. Lifshitz and A. Rotem, “Time-dependent longitudinal strength of unidirectional fibrous composites,” *Fibre Science and Technology,* vol. 3, no. 1, pp. 1-20, 1970.

[44] S. Blassiau, A. R. Bunsell and A. Thionnet, “Damage accumulation processes and life prediction in unidirectional composites,” *Proceedings of the Royal Society A,* vol. 463, no. 2080, pp. 1135-1152, 2007.

[45] A. R. Bunsell and A. Thionnet, “Life prediction for carbon fibre filament wound composite structures,” *Philosophical Magazine,* vol. 90, no. 31-32, pp. 4129-4146, 2010.

[46] A. R. Bunsell and A. Thionnet, “Failure processes governing long term reliability of carbon fibre composites structures,” *Composites and nanostructures,* vol. 7, no. 4, pp. 216-224, 2015.

[47] L. M. McGrath, R. S. Parnas, S. H. King, J. L. Schroeder, D. A. Fischer and J. L. Lenhart, “Investigation of the thermal, mechanical, and fracture properties of alumina-epoxy composites,” *Polymer,* vol. 49, no. 4, pp. 999-1014, 2008.

[48] C. Chen, R. S. Justice, D. W. Schaefer and J. W. Baur, “Highly dispersed nanosilica-epoxy resins with enhanced mechanical properties,” *Polymer,* vol. 49, no. 17, pp. 3805-3815, 2008.

[49] E. Schöberl, C. Breite, S. Rosini, Y. Swolfs, M. N. Mavrogordato, I. Sinclair and S. M. Spearing, “A novel particle-filled carbon-fibre reinforced polymer model composite tailored for the application of digital volume correlation and computed tomography,” *Manuscript in preparation,* 2020.

[50] Toray Industries Inc., *Toray Composite Materials,* Tokyo, Japan, 2019.

[51] US Research Nanomaterials Inc., *Micron Powders,* Houston, TX, USA, 2019.

[52] Sicomin, *Epoxy Systems,* Châteauneuf-les-Martigues, France, 2018.

[53] Ultrawave Ltd., *U100/U100H Ultrasonic Cleaning Bath,* Cardiff, UK, 2017.

[54] 3M Company, *Epoxy Adhesive,* Maplewood, MN, USA, 2019.

[55] Deben Ltd., *CT5000 5kN in-situ tensile stage for µXCT applications,* Woolpit, Suffolk, UK, 2019.

[56] LaVision GmbH, *DaVis v10 StrainMaster (Digital Volume Correlation),* Göttingen, Germany, 2018.

[57] E. M. C. Jones and M. A. Iadicola, "A good practices guide for digital image correlation," International Digital Image Correlation Society (iDICs), 2018.

[58] A. Buljac, T. Taillandier-Thomas, L. Helfen, T. F. Morgeneyer and F. Hild, "Evaluation of measurement uncertainties of digital volume correlation applied to laminography data," *The Journal of Strain Analysis,* vol. 53, no. 2, pp. 49-65, 2018.

[59] H. L. Cox, "The elasticity and strength of paper and other fibrous materials," *British Journal of Applied Physics,* vol. 3, no. 3, pp. 72-79, 1952.

[60] W. Voigt, "Ueber die Beziehung zwischen den beiden Elasticitätsconstanten isotroper Körper," *Annalen der Physik,* vol. 274, no. 12, pp. 573-587, 1889.

[61] B. W. Kim and J. A. Nairn, "Observations of fiber fracture and interfacial debonding phenomena using the fragmentation test in single fiber composites," *Journal of Composite Materials,* vol. 36, no. 5, pp. 1825-1858, 2002.

[62] B. W. Kim and J. A. Nairn, "Experimental verification of the effects of friction and residual stress on the analysis of interfacial debonding and toughness in single fiber composites," *Journal of Materials Science,* vol. 37, no. 18, pp. 3965-3972, 2002.

[63] Z. Yang, B. Zhang, L. Zhao and X. Sun, "Stress transfer around a broken fiber in unidirectional fiber-reinforced composites considering matrix damage evolution and interface slipping," *Science China Physics, Mechanics and Astronomy,* vol. 54, no. 2, pp. 296-302, 2011.

[64] A. N. Netravali, R. B. Henstenburg, S. L. Phoenix and P. Schwartz, "Interfacial shear strength studies using the single-filament-composite test. I: Experiments on graphite fibers in epoxy," *Polymer Composites,* vol. 10, no. 4, pp. 226-241, 1989.

[65] A. Pegoretti, M. L. Accorsi and A. T. Dibenedetto, "Fracture toughness of the fibre-matrix interface in glass-epoxy composites," *Journal of Materials Science,* vol. 31, no. 23, pp. 6145-6153, 1996.

[66] F. M. Zhao and N. Takeda, "Effect of interfacial adhesion and statistical fiber strength on tensile strength of unidirectional glass fiber/epoxy composites. Part I: experiment results," *Composites Part A,* vol. 31, no. 11, pp. 1203-1214, 2000.

[67] Y. Swolfs, R. M. McMeeking, I. Verpoest and L. Gorbatikh, "Matrix cracks around fibre breaks and their effect on stress redistribution and failure development in unidirectional composites," *Composites Science and Technology,* vol. 108, pp. 16-22, 2015.

[68] X. Ji, X. R. Liu and T. W. Chou, "Dynamic stress concentration factors in unidirectional composites," *Journal of Composite Materials,* vol. 19, no. 3, pp. 269-275, 1985.

[69] S. L. Phoenix and I. J. Beyerlein, Comprehensive composite materials. Chapter 1.19 – Statistical strength theory for fibrous composite materials, 1st ed., vol. 1, A. Kelly and C. Zweben, Eds., Oxford, UK: Pergamon Press, 2000, pp. 559-639.

[70] R. P. Tavares, F. Otero, J. Baiges, A. Turon and P. P. Camanho, “A dynamic spring element model for the prediction of longitudinal failure of polymer composites,” *Computational Materials Science,* vol. 160, pp. 42-52, 2019.

[71] A. E. Scott, I. Sinclair, S. M. Spearing, M. N. Mavrogordato and W. Hepples, “Influence of voids on damage mechanisms in carbon/epoxy composites determined via high resolution computed tomography,” *Composites Science and Technology,* vol. 90, pp. 147-153, 2014.

[72] T. Hobbiebrunken, B. Fiedler, M. Hojo and M. Tanaka, “Experimental determination of the true epoxy resin strength using micro-scaled specimens,” *Composites Part A,* vol. 38, no. 3, pp. 814-818, 2007.

[73] Y. Swolfs, C. Breite, S. V. Lomov and L. Gorbatikh, “Fibre break interactions in unidirectional composites under longitudinal tensile loading,” in *The 7th European Community on Computational Methods in Applied Sciences*, Girona, Spain, 2019.

[74] A. Kelly and W. R. Tyson, “Tensile properties of fibre-reinforced metals: Copper/tungsten and copper/molybdenum,” *Journal of the Mechanics and Physics of Solids,* vol. 13, no. 6, pp. 329-350, 1965.

[75] S. Pimenta and S. T. Pinho, “Hierarchical scaling law for the strength of composite fibre bundles,” *Journal of the Mechanics and Physics of Solids,* vol. 61, no. 6, pp. 1337-1356, 2013.

[76] S. Pimenta, “A computationally-efficient hierarchical scaling law to predict damage accumulation in composite fibre-bundles,” *Composites Science and Technology,* vol. 146, pp. 210-225, 2017.

[77] A. Bunsell, L. Gorbatikh, H. Morton, S. Pimenta, I. Sinclair, S. M. Spearing, Y. Swolfs and A. Thionnet, “Benchmarking of strength models for unidirectional composites under longitudinal tension,” *Composites Part A,* vol. 111, pp. 138-150, 2018.

[78] M. R. Wisnom and D. Green, “Tensile failure due to interaction between fibre breaks,” *Composites,* vol. 26, no. 7, pp. 499-508, 1995.

[79] S. Yaofeng and J. H. L. Pang, “Study of optimal subset size in digital imagecorrelation of speckle pattern images,” *Optics and Lasers in Engineering,* vol. 45, no. 9, pp. 967-974, 2007.

[80] J. Schindelin, I. Arganda-Carreras, E. Frise, V. Kaynig, M. Longair, T. Pietzsch, S. Preibisch, C. Rueden, S. Saalfeld, B. Schmid, J.-Y. Tinevez, D. J. White, V. Hartenstein, K. Eliceiri, P. Tomancak and A. Cardona, “Fiji: an open-source platform for biological-image analysis,” *Nature Methods,* vol. 9, pp. 676-682, 2012.

[81] O. Jiroušek, I. Jandejsek and D. Vavřík, “Evaluation of strain field in microstructures using micro-CT and digital volume correlation,” in *The 12th International Workshop on Radiation Imaging Detectors*, Cambridge, UK, 2010.